JOURNAL OF GEOPHYSICAL RESEARCH, VOL. 101, NO. E1, PAGES 2177–2200, JANUARY 25, 1996

The magnetic fields of Uranus and Neptune: Methods and models

Richard Holme[1] and Jeremy Bloxham
Department of Earth and Planetary Sciences, Harvard University, Cambridge, Massachusetts

Abstract. We present new models of the magnetic fields of Uranus and Neptune, based on data provided by the Voyager II magnetic field experiment. We find the simplest models that satisfy the data, and use the observed surface heat flow as a constraint on the magnetic field structure. Our models are similar to the previously described Q_3 and O_8 models far from the planets, but resolve smaller-scale structure close to the planets' surfaces. The field of Neptune is much better constrained than that of Uranus, and the field in the northern hemisphere of Neptune is much better constrained than that in the southern hemisphere, of importance for studies of Neptunian northern hemisphere radio sources. Using extremal models, we show that the large dipole tilts and nondipole dominance of the fields are robust features required by the data. Scaling analysis suggests that the toroidal field that would be required for a magnetostrophic balance in the dynamo region would result in ohmic dissipation greater than the observed surface heat flow. Thus we suggest that the dynamos of Uranus and Neptune are energy limited, and that the subsequent lack of magnetostrophic balance may account for the radically different field morphologies of Uranus and Neptune compared with the Earth, Jupiter, and Saturn.

Introduction

Six planets in the solar system possess strong magnetic fields of internal origin [*Russell*, 1993; *Connerney*, 1993] maintained by dynamo action. The fields of the Earth, Mercury, Jupiter, and Saturn are dominantly dipolar, with strong symmetry about the rotation axis, features which prior to 1986 were the accepted paradigm for the morphology of planetary fields. However, the Voyager II encounter with Uranus revealed a very different field geometry, with no obvious axial symmetry, and significant higher-degree structure. Initial explanations for the unusual field appealed to the anomalous tilt of Uranus, or suggested that the field might be reversing, but such ad hoc mechanisms became less attractive with the observation of similar field structure at Neptune. Instead, we must now explain the existence of two very different classes of planetary magnetic fields. The purpose of this paper is to examine this second class of planetary magnetic fields by further analysis of the data taken by Voyager II at Uranus and Neptune, and to provide possible explanations for their nature.

[1]Now at Department of Geology and Geophysics, University of Edinburgh, Scotland.

Paper number 95JE03437.
0148-0227/96/95JE-03437$05.00

The magnetic field in an electrical insulator can be written $\mathbf{B} = -\nabla\Phi$, where Φ is a scalar potential satisfying Laplace's equation $\nabla^2\Phi = 0$. In spherical geometry, the solution for the internal planetary field is

$$\Phi = a\sum_{l=1}^{\infty}\left(\frac{a}{r}\right)^{l+1}\sum_{m=0}^{l}P_l^m(\cos\theta) \times [g_l^m\cos(m\phi) + h_l^m\sin(m\phi)] \quad (1)$$

where a is the radius of the planet and (r,θ,ϕ) is a planetocentric spherical coordinate system. $P_l^m(\cos\theta)$ are Legendre polynomials, by convention Schmidt normalized, so that

$$\int_{\phi=0}^{2\pi}\int_{\theta=0}^{\pi}(P_l^m(\cos\theta)\cos m\phi)^2\sin\theta d\theta d\phi = \frac{4\pi}{2l+1} \quad (2)$$

We use the measurements of the magnetic field to estimate the coefficients g_l^m and h_l^m, called the Gauss coefficients, which then uniquely define the planetary field external to the source (conducting) region in the planet.

Because the data are restricted to the path of the spacecraft, they are sparse and unevenly distributed. Further, many of the measurements were taken far from the planet, and so do not sample high-degree ($l > 1$) harmonics well. *Connerney* [1981] has shown that it is possible to construct fields which are of significant magnitude at the surfaces of the planets, but which would

have been undetectable by the spacecraft: this illustrates the nonuniqueness in any field model that we may obtain from the data, a serious problem in modeling all fields, but which is particularly significant here because data are only available from a single flypast of each planet.

Connerney et al. [1987, 1991] obtained values for the Gauss coefficients using a method based on singular value decomposition (SVD) [*Lanczos*, 1961; *Connerney*, 1981]. They truncated the spherical harmonic expansion equation (1) and determined a solution using a generalized eigenvalue analysis. If an eigenvector has eigenvalue 0, then the linear combination of coefficients defined by that eigenvector has no effect on the data, and the vector is part of the null space. *Connerney et al.* [1987, 1991] chose their truncation level to be the minimum that allows an adequate fit to the data, leading to truncation at degree 3 for Uranus, and degree 8 for Neptune. They discarded eigenvectors with small, but nonzero eigenvalues, thereby extending the null space. Then coefficients above degree 2 for Uranus and degree 3 for Neptune were discarded as being inadequately resolved. This has the unfortunate consequences that available information concerning higher-degree components of the field is lost, and that the final models (Q_3 and O_8) do not fit the data (although, of course, the full solutions including the poorly resolved higher-degree coefficients do fit the data). Our approach is instead to solve for fields to high degree, and to resolve the nonuniqueness by seeking fields with certain desirable properties, such as smoothness, or low field strength, electrical heating, or stored energy. This enables us to say something about higher-degree components of the field, and to test hypotheses about the nature of the field directly against the data.

In this paper, we begin by describing the available data for modeling the fields of Uranus and Neptune, and techniques we have used to average and cull the raw data to obtain a data set for inversion. We then describe the method that we use to estimate the field coefficients from this data set, including the use of a bound on the ohmic heating as a modeling constraint. This procedure results in a number of models of the magnetic fields of Uranus and Neptune: we present these both as maps of the field and as power spectra. We then explore the range of permissible models that are consistent with the data, and use extremal modeling to examine the robustness of the large dipole tilts, the form of the spectra, and the general symmetry properties of the models. Finally, we present some simple analyses of the dynamics to explore possible mechanisms for the unusual field morphology.

Data

Voyager II was within the magnetosphere of Uranus for 16 hours, and that of Neptune for 38 hours, during which periods three orthogonal components of the magnetic field were recorded without significant interruption. The trajectories followed by the spacecraft are shown in Figure 1. The instrumentation, described in detail by *Behannon et al.* [1977], included both low flux (LFM) and high flux (HFM) magnetometers, sensitive to different field strengths, which switched automatically between different ranges of sensitivity depending on the measured field strength. Only the LFM was used during the Uranus encounter, but the measurements near closest approach of Neptune also used the HFM. After correction for the intrinsic spacecraft field using a dual magnetometer technique [*Ness et al.*, 1971], the data from both encounters were deposited at the National Space Science Data Center (NSSDC), Greenbelt, Maryland, by the Voyager magnetic field investigation team (N. F. Ness, principal investigator). With no new missions to either planet currently under consideration, it is unlikely that the available data will be augmented in the near future.

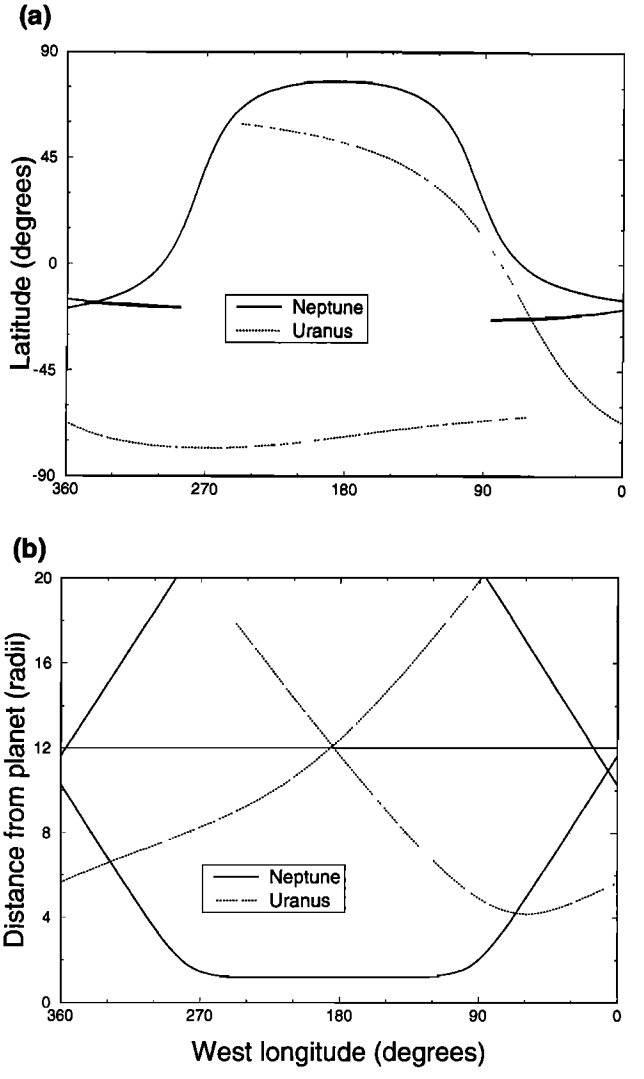

Figure 1. Spacecraft trajectories. (a) Latitude versus longitude. (b) Distance versus longitude (Horizontal lines mark outer radial extent of data used for inversions).

Data Errors

The measured field is the sum of contributions from both internal (planetary) and external (magnetospheric) sources. We may formally expand for external sources of magnetic field in a manner similar to the expansion for the internal field in equation (1). However, such external terms have a growing radial dependence, and inspection of the data shows that the fields of both planets decay rapidly with increasing r. There is no evidence for strong magnetospheric sources at Uranus or Neptune, such as the ring currents which complicate the determination of the internal field of Jupiter [*Connerney et al.*, 1981]. We model the external field from magnetospheric sources as a small constant field, with scalar potential

$$\Phi = a\left(G_1^0 \cos\theta + G_1^1 \sin\theta\cos\phi + H_1^1 \sin\theta\sin\phi\right) \quad (3)$$

and assume variations in its strength are sufficiently rapid to be modeled as Gaussian noise, with magnitude 0.5 nT for Uranus and 1.0 nT for Neptune, estimated from the value of the solar field just prior to encounter. This is the dominant source of error in the field measurements far from the planets.

The instrument precision varies as the magnetometers switch automatically between their different sensitivity ranges. The limit of resolution is stated to be approximately 0.05 nT + 0.1% of full scale, where full scale varies from 8.8 nT, through 2100 nT (precision 0.51 nT) at closest approach to Uranus, to 50000 nT (precision 26 nT) for the HFM at closest approach to Neptune. The data returned by each instrument are not smooth: a constant value is recorded until the threshold of the next quantized step is reached. However, field components in the planetocentric frame appear to vary smoothly as a consequence of the smooth rotation of the spacecraft with respect to the planetocentric frame. Further details of the instrument response are given by *Ness et al.* [1986, 1989] and *Connerney et al.* [1987, 1991].

Further uncertainty in the measurements arises from errors in the determination of the position and attitude of the spacecraft. Whilst examination of the data suggests that errors in position are small, attitude errors are more significant. *Connerney et al.* [1987, 1991] report that the attitude was in general determined to within 0.05° during the Uranus encounter, and to 0.1° during the Neptune encounter, making this source of error potentially comparable to that from instrument sensitivity. In addition, there were short periods during spacecraft maneuvers when the uncertainty was much greater, and only measurements of total intensity can be used. A more complete treatment of attitude errors is given by *Holme and Bloxham* [1995], and is described briefly below.

Data Smoothing

Voyager II returned values of the magnetic field at an interval between 0.06 and 0.6 s. On this short timescale, the data are highly redundant, and their errors are highly correlated. In previous studies, these data were either time averaged [*Connerney et al.*, 1987] using an iterative data adaptive sorting scheme (J. E. Connerney, personal communication, 1993), or culled without averaging [*Connerney et al.*, 1991]. Neither of these approaches is entirely satisfactory. Averaging over extended times introduces spatial bias to the measurements, and, as noted by *Davis and Smith* [1990], will tend to overvalue the uncertainty, whilst culling discards most of the data, with potential loss of information. Instead, we determine a continuous running average for each field component, by fitting a smooth curve through each component using penalized least squares splines [*Constable and Parker*, 1988, 1991].

We seek the smoothest function $f(x)$ which provides a specified fit to the data $\{y_i\}$, standard deviation $\{\sigma_i\}$, by minimizing the functional

$$F = \sum_{i=1}^{N} \frac{(y_i - f(x_i))^2}{\sigma_i^2} + \lambda \int f''(x)^2 dx \quad (4)$$

The solution to this problem is well known to be a set of piecewise cubic polynomials, called smoothing splines, joined at the locations of the data points $\{x_i\}$, called the knots. For a large number of data, the calculation of these functions becomes intractable. *Constable and Parker* [1988] suggested an alternative method, called penalized least squares splines, based on the construction of a more widely spaced knot sequence x_k, upon which the smooth function is constructed on a basis of cubic B-splines. The ith cubic B-spline is such that $B_i(x) > 0$ if $x_k < x < x_{k+4}$ and zero otherwise, and the sum of the B-splines at any point is unity. B-splines are described in more detail by *de Boor* [1978]. In Figure 2, we illustrate the B-spline basis for a simple case with uniformly spaced knots (as used in our calculations). We solve for the set of B-spline coefficients that minimize the functional F, subject to a desired fit to the data, obtained by varying the damping parameter λ. This problem can be posed in matrix form, and be-

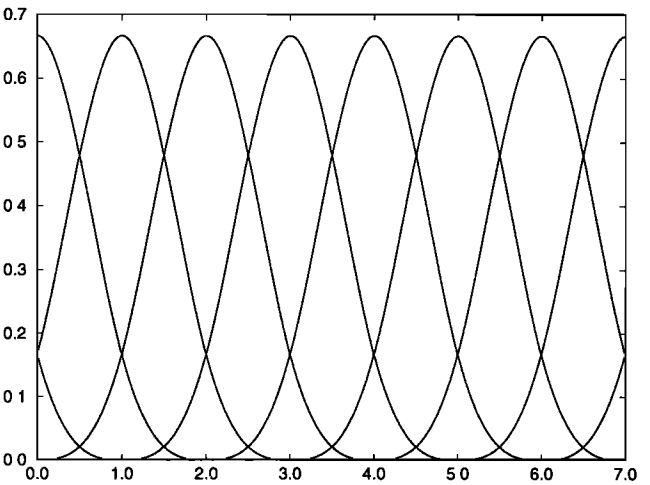

Figure 2. A B-spline basis for evenly spaced knots.

cause the B-splines are only locally nonzero, the matrices are banded, allowing efficient solution. To achieve a good approximation to the smoothing splines solution, we must choose sufficient knots that the smooth function is controlled by the damping, and not by the number of knots. For further details, see *Constable and Parker* [1988].

Our procedure for smoothing the data consists of several steps. First, we detrend the data. We fit the Uranus data using simple least squares with a truncated spherical harmonic expansion of degree and order 3, and then subtract this field from each component time series.

Second, we find the penalized spline fit to the detrended data. To do this, we treat the standard deviations $\{\sigma_i\}$ of the data as unknown, but constant within each magnetometer sensitivity range. Then we solve for the B-spline coefficients for a range of λ, iteratively seeking a self-consistent solution for which the variance in each range is equal to the data mean square misfit, and construct a trade-off curve by plotting the "roughness" $\left(\int f''(x)^2 dx\right)$ against the normalized misfit. We look for a "knee" (a sharp change in slope) in this curve, and adopt the corresponding value of λ as our optimal solution. Ideally, increasing the damping parameter above this value would produce little improvement in smoothness at the cost of significantly worsening the fit to the data, while decreasing the damping parameter would give a much rougher solution for little reduction in misfit.

Last, we reconstruct the data by adding this smooth function to the trend removed by the simple degree 3 fit, to produce continuous smooth functions for the three magnetic field components.

To construct our magnetic field data set, we then sample these smooth functions. One approach would be simply to sample uniformly in time, but this would give data with highly uneven spatial separation, and, in particular, comparatively poor coverage near closest approach, where we expect the most informative data to be located. Note, however, that selecting too many points near closest approach unduly biases the inversion against fitting the data elsewhere. The information content of a particular datum is described by the Green's function for the problem [*Gubbins and Roberts*, 1983]. We examine the correlation between the Green's functions of successive data points, and find that a simple strategy of adopting data with constant angular separation does not bias the inversion. Finally, we note that when the spacecraft attitude is not known, we should not use the values predicted by our smooth function, but must instead use total intensity data only.

Summary of the Data Sets Used for Modeling

We received the Uranus data in the form of 1.96 s averages of each component. We averaged these data using the technique described above, with 6000 splines being sufficient to fit 32,000 data. We then sampled at 0.5° angular separation and assigned each point an error of 0.5 nT, since after smoothing, the errors from the external fields dominate instrument uncertainty. Data at further than $8R_U$ from the planet (see Figure 1) were discarded because of contamination from external fields.

The errors in the Neptune data are dominated by limits to instrument precision, and thus our smooth averaging technique should have been extremely useful. Unfortunately, the data from the Neptune encounter were only available in highly decimated form, providing insufficient temporal resolution to apply the spline technique, so we use the data set described by *Connerney et al.* [1991]. We use data within a radius of $12R_N$, again to reduce effects of external fields. We follow *Connerney et al.* [1991] in adopting the instrument quantization precision σ as relative weights to allow for all sources of error in the data (the error from the quantization error alone is uniformly distributed with variance $\sigma^2/12$). The postulated error varies from 1.0 nT (approximating external fields) at $12R_N$, to 26 nT near closest approach.

Method

Our aim is to determine the magnetic fields of Uranus and Neptune from the available data. From equation (1) the problem might appear to be simply one of parameter estimation, in other words one of simply determining the Gauss coefficients which uniquely define the planetary field external to the source (conducting) region in the planet. However, the field is described by an infinite number of Gauss coefficients, and since we have an unavoidably finite number of data, we must exercise some care in how we seek to estimate a finite subset of the coefficients. Our approach is to seek to estimate the field subject to an additional smoothing constraint.

Following *Whaler and Gubbins* [1981] and *Gubbins* [1983], if the errors in the data are assumed Gaussian with zero mean, then to optimize the fit to the data, we should minimize

$$\mathbf{e}^{\mathrm{T}}\mathbf{C_e}^{-1}\mathbf{e}, \tag{5}$$

where $\mathbf{C_e}$ is the data covariance matrix for the errors

$$(C_e)_{ij} = \mathrm{cov}(e_i, e_j) \tag{6}$$

and the error vector $\mathbf{e}$ is given by

$$\mathbf{e} = \boldsymbol{\gamma} - \mathbf{Am} \tag{7}$$

where $\mathbf{A}$ is an operator calculated from equation (1) relating the data vector $\boldsymbol{\gamma}$ to the model vector $\mathbf{m}$. We assume that all the data are linearly related to the model (for example, the three orthogonal magnetic field components rather than total field intensity): the extension of the method to deal with nonlinear data is given by *Gubbins and Bloxham* [1985].

In addition, following *Shure et al.* [1982], we seek fields which are smooth over a volume or surface. For example, we might choose to minimize

$$\langle \mathbf{B}.\mathbf{B} \rangle_r = \sum_{l=1}^{\infty} (l+1) \left(\frac{a}{r}\right)^{2l+4} \sum_{m=0}^{l} \left((g_l^m)^2 + (h_l^m)^2\right) \quad (8)$$

the mean field strength averaged over a spherical surface, radius r [*Lowes*, 1966]. We may express this quantity and others like it as a quadratic norm

$$\mathbf{m}^{\mathrm{T}} \mathbf{\Lambda} \mathbf{m} \quad (9)$$

where $\mathbf{\Lambda}$ is a positive definite matrix, in this case with diagonal elements

$$f(l,r) = (l+1)\left(\frac{a}{r}\right)^{2l+4} \quad (10)$$

and zeros elsewhere.

We minimize the functional

$$(\gamma - \mathbf{A}\mathbf{m})^{\mathrm{T}} \mathbf{C_e}^{-1} (\gamma - \mathbf{A}\mathbf{m}) + \lambda \mathbf{m}^{\mathrm{T}} \mathbf{\Lambda} \mathbf{m} \quad (11)$$

where λ is a Lagrange multiplier. The maximum likelihood solution is

$$\hat{\mathbf{m}} = (\mathbf{A}^{\mathrm{T}} \mathbf{C_e}^{-1} \mathbf{A} + \lambda \mathbf{\Lambda})^{-1} \mathbf{A}^{\mathrm{T}} \mathbf{C_e}^{-1} \gamma \quad (12)$$

The matrix $(\mathbf{A}^{\mathrm{T}} \mathbf{C_e}^{-1} \mathbf{A} + \lambda \mathbf{\Lambda})$ is real symmetric and positive definite, and so the solution to equation (12) can be obtained efficiently by, for example, Cholesky decomposition. In practice, we vary the Lagrange multiplier until we obtain the required fit to the data. Because the true value of the constraint and fit to the data are unknown, we plot a trade-off curve of the value of the norm against the misfit to the data, and adopt the value of λ at the "knee" of the curve.

A common alternative to smoothing is to truncate the spherical harmonic series. This can be considered as a particularly severe form of damping, in which $\mathbf{\Lambda}$ is diagonal, with elements 0 for the nontruncated terms, and infinity for the truncated terms. In practice, we too must truncate the expansion, but we do so at a sufficiently high-degree so as not to affect the solution. Convergence and high-degree coefficients are determined by the properties of the norm, rather than choice of truncation level.

Data Error Covariance Matrix

The data error covariance matrix expresses our degree of confidence in the observations. The uncertainty arises from a combination of external field noise and instrument error, both assumed isotropic, with combined variance σ^2, and attitude uncertainty, with angular variance ψ^2. As a result of the attitude uncertainty, the errors in the orthogonal field components are nonisotropic and correlated. The covariance matrix for each triplet of field components is given by

$$\mathbf{C_e} = \mathbf{I}(\sigma^2 + B^2\psi^2) - \mathbf{B}\mathbf{B}^{\mathrm{T}}\psi^2 \quad (13)$$

[*Holme and Bloxham*, 1995], which has inverse

$$\mathbf{C_e}^{-1} = \frac{\left(\mathbf{I}\sigma^2 + \mathbf{B}\mathbf{B}^{\mathrm{T}}\psi^2\right)}{\sigma^2(\sigma^2 + B^2\psi^2)} \quad (14)$$

In common with *Connerney et al.* [1987, 1991], we assume $\sigma = 0.5$ nT at closest approach to Uranus, where the field magnitude $B = 411$ nT, and 26 nT at closest approach to Neptune, where $B = 9940$ nT. The orientation is supposed known to 0.05° for Uranus, and 0.1° for Neptune, so $B\psi = 0.36$ nT for Uranus, and $B\psi = 17$ nT for Neptune. These estimates are comparable to the estimated instrument error, so in principle we must consider the possible effects of a nondiagonal covariance matrix when inverting the data. However, due to poor data coverage, the effects of the error correlation were much less than the effect of small variations in the damping parameter λ.

Smoothing Norms

We have used a variety of smoothing norms in this study, listed in Table 1, all of which yield diagonal

Table 1. Smoothing Norms for Magnetic Field Inversions

	Integral to Minimize	Norm Function $f(l, r_0)$
(a)	$\oint B^2 d\Omega \Big\|_{r=r_0}$	$(l+1)\left(\frac{a}{r_0}\right)^{(2l+4)}$
(b)	$\oint B_r^2 d\Omega \Big\|_{r=r_0}$	$\frac{(l+1)^2}{2l+1}\left(\frac{a}{r_0}\right)^{(2l+4)}$
(c)	$\oint (\nabla_H B_r)^2 d\Omega \Big\|_{r=r_0}$	$\frac{l(l+1)^3}{2l+1}\left(\frac{a}{r_0}\right)^{(2l+6)}$
(d)	$\int B^2/\mu_0 dV \Big\|_{r>r_0}$	$\frac{l+1}{2l+1}\left(\frac{a}{r_0}\right)^{(2l+1)}$
(e)	$\int J^2/\sigma dV \Big\|_{r<r_0}$	See equation (16)

Note the additional factor of $(2l+1)$ in (a)-(c) from *Shure et al.* [1982], to allow for Schmidt normalization.

damping matrices. Norm (a) is the minimum field strength expression described in equation (8) above, while norms (b) and (c) follow *Shure et al.* [1982], minimizing the mean square radial field and its horizontal derivative respectively. Norm (d) minimizes the energy of the magnetostatic field external to the planet [e.g., *Benton and Alldredge*, 1987; *Rädler and Ness*, 1990].

Norm (e) is derived from a constraint on the ohmic dissipation of the magnetic field. *Gubbins* [1975] showed that for a uniform conductivity core and a known potential field, there is a unique internal current distribution (and hence field) that generates the minimum ohmic heat. In Appendix A we extend this result to allow for radial variations in conductivity. This places a lower bound on the ohmic heating associated with the observed field and, if used as a smoothing constraint, yields fields with the smallest possible value of this lower bound. In order to apply this norm, we need to consider the internal structure and conductivity profiles of Uranus and Neptune.

Radial Conductivity Profiles

The detailed internal structures of Uranus and Neptune are not known. Models are customarily proposed with three compositionally distinct polytropic layers: "gas" (predominantly hydrogen and helium), "ice" (predominantly water and ammonia), and "rock" (iron and silicates), although sharp compositional boundaries are not required and are in fact unlikely. As the pressure in the gas regions is too low to form metallic hydrogen [*Hubbard and MacFarlane*, 1980], the magnetic fields are assumed to originate in the ionically conducting icy mantles. Shock wave experiments [*Nellis et al.*, 1988] suggest that the ionic conductivity of "synthetic Uranus" (a mixture of C,H,O,N in proportions derived from cosmochemical arguments) increases with pressure until it saturates at a value of 2×10^3 S m^{-1} at 40GPa (compare this with 3×10^5 S m^{-1}, a commonly used value for the conductivity of the Earth's core [*Stacey*, 1992, section 7.2.3]). Simple modeling combining the experimental pressure-conductivity relation with interior models of the two planets [*Podolak et al.*, 1990, 1995; *Hubbard et al.*, 1991] suggests an approximate conductivity profile

$$\begin{aligned} \sigma &= \sigma_0 & r &< c \\ \sigma &= \sigma_0 \left(\frac{b-r}{b-c}\right) & c &< r < b \\ \sigma &= 0 & r &> b \end{aligned} \qquad (15)$$

where σ_0 is the saturation conductivity, c is the saturation depth (taken to be about $0.7R_U$ and $0.75R_N$), and b is the depth at which conductivity is negligible (approximately $c + R/10$). Our results are insensitive to the precise details of the conductivity profile, the linear form being adopted for reasons of convenience. Using equation (A15), we obtain a lower bound on the heat generated

$$W_B \geq 4\pi \sum_{l,m} \left\{ \frac{a^{2l+4}}{\mu_0^2 \sigma_0} \frac{(l+1)(2l+1)(2l+3)(2l+4)}{l} \times \frac{(b-c)}{(b^{2l+4} - c^{2l+4})} ((g_l^m)^2 + (h_l^m)^2) \right\} \qquad (16)$$

from which we construct our smoothing norm.

Constraining the Field Structure by Ohmic Heating

In addition to regularizing the inverse problem, we may hope to gain additional insight by comparing the ohmic heating bound calculated from a model with the observed surface heat flow. By considering the dynamo as a heat engine, *Hewitt et al.* [1975] and *Backus* [1975] showed that the ohmic dissipation from a dynamo driven by thermal convection is bounded by

$$W_B \leq \left(\frac{T_m - T_o}{T_o}\right) Q_o \qquad (17)$$

Here T_m is the maximum temperature within the dynamo, T_o is the temperature at the outer boundary, and Q_o is the heat flow from the dynamo region. *Hubbard et al.* [1991] give temperature values for Neptune of 3000 K at the top of the icy region and 7000 K for the center of the planet. The dynamo region is somewhat below the surface of the icy region: we adopt a temperature of 3500 K as representative of this depth. The heat flow out of the dynamo region is probably close to, and certainly bounded by, the observed surface heat flow. With these numbers, equation (17) gives $W_B \leq Q_S$, i.e., the ohmic heating is bounded by the surface heat flow, a result which is also consistent with the temperature profiles of the recent models of *Podolak et al.* [1995]. This simple relation would be invalidated by significant compositional convection [*Gubbins*, 1977], thought to be important in driving the Earth's dynamo [*Gubbins et al.*, 1979].

In Uranus and Neptune, Lindemann's law [*Hubbard*, 1981] suggests that the dynamo region is fully liquid, whilst a Fe/Mg silicate core is fully solid (although a multiple component system may have a lower melting point). With no obvious process to drive compositional convection, we assume the dynamos are thermally driven, so that equation (17) is valid. We are also assuming a thermodynamic steady state. Heat generated deep within the planet by electrical currents will take time to reach the surface through processes of conduction and convection, so the surface heat flow observed today is characteristic of past fields. We must assume variations in heat production average out over time.

We divide the internal magnetic field into toroidal and poloidal parts [e.g., *Gubbins and Roberts*, 1987]:

$$\mathbf{B} = \nabla \wedge T\mathbf{r} + \nabla \wedge \nabla \wedge P\mathbf{r} \qquad (18)$$

where T and P are the toroidal and poloidal scalars. From the orthogonality of toroidal and poloidal fields

over a sphere [*Bullard and Gellman*, 1954], the magnetic heating also splits into two parts

$$W_B = W_T + W_P \tag{19}$$

where W_T is the ohmic heating due to poloidal currents associated with the toroidal field B_T, and W_P is the ohmic heating due to toroidal currents associated with poloidal field B_P. Because the toroidal field must be zero outside the conducting region, the magnetic field observations, and hence the ohmic heating norm, only provide a direct constraint on W_P. However, it is commonly assumed that in the dynamo region $B_T \gg B_P$ and so $W_T \gg W_P$. We return to this issue below. Further, the ohmic heating norm is only a lower bound on the poloidal heat generation, based on the observed field, which in turn does not include small-scale (high-degree) structure which is highly attenuated by distance from the planet, but may still contribute significantly to ohmic heating. Thus we do not expect the ohmic heating bound to provide a strong constraint on the structure of the field, although it will prove useful in extremal modeling.

Resolution Analysis

The extent to which the field model is determined by the data is described by the resolution matrix

$$\mathbf{R} = (\mathbf{A}^{\mathrm{T}}\mathbf{C_e}^{-1}\mathbf{A} + \lambda\mathbf{\Lambda})^{-1}\mathbf{A}^{\mathrm{T}}\mathbf{C_e}^{-1}\mathbf{A} \tag{20}$$

If λ is very small, then all parameters are determined solely by the data, and $\mathbf{R} = \mathbf{I}$. If a diagonal element of $\mathbf{R}$ is close to 1, and nondiagonal elements are small, we say that the corresponding coefficient is "well-resolved", meaning that its value is specified solely by the data, independently of other coefficients. If non-diagonal elements are large, then the estimates of the different coefficients are not independent. At high degree, the coefficients are determined solely by the norm, and the elements of the resolution matrix are zero.

It is important to realize that just because a coefficient is well resolved, it is not necessarily well determined. An estimate of the uncertainties in the model can be obtained from the covariance matrix

$$\mathbf{C} = \hat{\sigma}^2(\mathbf{A}^{\mathrm{T}}\mathbf{C_e}^{-1}\mathbf{A} + \lambda\mathbf{\Lambda})^{-1} \tag{21}$$

where

$$\hat{\sigma}^2 = \mathbf{e}^{\mathrm{T}}\mathbf{C_e}^{-1}\mathbf{e}/[N - \mathrm{tr}(\mathbf{R})] \tag{22}$$

and N is the number of data. However, when properly interpreted within the framework of Bayesian inference [*Backus*, 1988; *Bloxham et al.*, 1989], the covariance estimate is revealed to be good only if we believe that the value of the smoothing norm of the true field is bounded by that of our calculated model. We make no such claim: our fields are the smoothest possible in some sense, but we do not claim such smoothness is required. In practice, the uncertainties in the coefficients are best explored through synthetic experiments, described below.

Results

We have obtained a variety of models for the fields of Uranus and Neptune, all of which provide a good fit to the data and possess additional desirable properties. As representative choices, we present models calculated with the ohmic heating norm, which we designate Umoh and Nmoh. In Figure 3 we show trade-off curves for both data sets, normalizing the data misfit to the nominal uncertainty, and the value of the norm to the observed surface heat flow Q_S ($0.34 \pm 0.38 \times 10^{15}$ W for Uranus and $3.3 \pm 0.35 \times 10^{15}$ W for Neptune [*Pearl and Conrath*, 1991]). In both cases the knee in the trade-off curve is clearly visible and also robust to rescaling of the axes. The position of the knee is somewhat better defined for Neptune than for Uranus because the data have been decimated rather than averaged, and so our ability to fit the data is strongly limited by the size of the instrument error. With access to a data set with greater sampling frequency for Neptune, so that we could apply our spline techniques, we would expect to be able to say more about higher-degree structure. For our chosen models, the Uranus model Umoh fits the data to 0.6σ (0.3 nT), with $W_P \geq 3.3 \times 10^{10}$ W, while the Neptune model Nmoh fits the data to 0.8σ, with $W_P \geq 3.9 \times 10^{10}$ W. All of our models have ohmic heating norms well below Q_S and so, as expected, the observed surface heat flow does not strongly constrain optimally smooth models.

We present values for the spherical harmonic coefficients in Table 2. The three external source coefficients (corresponding to a constant field) are listed at the end of the table. Each coefficient set forms one possible field model (of many) which is well-behaved at the surface of

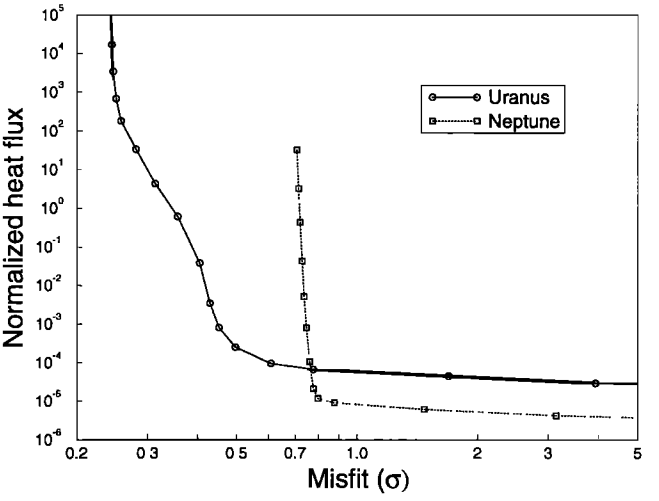

Figure 3. Trade-off curves between data misfit and ohmic heating norm. Heat flow bounds are normalized to the observed surface heat flows; misfit in nominal σ.

Table 2. Magnetic Field Coefficients for Models Umoh (Uranus) and Nmoh (Neptune)

		Uranus		Neptune				Uranus		Neptune	
l	m	g_l^m	h_l^m	g_l^m	h_l^m	l	m	g_l^m	h_l^m	g_l^m	h_l^m
1	0	11854.69		10335.72		12	0	0.00		35.19	
1	1	11507.23	-15811.90	3558.89	-9772.35	12	1	0.00	0.00	-16.82	-81.58
2	0	-5877.08		8565.94		12	2	0.00	0.00	114.25	-17.20
2	1	-13084.90	5850.66	-405.99	11138.62	12	3	0.00	0.00	-62.07	-48.73
2	2	-604.66	4184.69	4643.56	-743.14	12	4	0.00	0.00	33.69	-28.68
3	0	4182.82		-5749.29		12	5	0.00	0.00	0.81	-57.61
3	1	-1335.73	-5816.66	11631.96	-3904.67	12	6	0.00	0.00	52.25	-14.81
3	2	-6776.28	-357.27	-1888.70	902.89	12	7	0.00	0.00	-5.57	89.58
3	3	-4021.38	-2265.15	-2920.49	-245.31	12	8	0.00	0.00	10.36	-96.77
4	0	398.37		1851.87		12	9	0.00	0.00	-59.35	72.68
4	1	-431.86	-1013.87	1331.63	-2139.60	12	10	0.00	0.00	40.20	-29.67
4	2	2168.91	414.66	5410.37	3233.01	12	11	0.00	0.00	-12.44	-13.10
4	3	465.44	-637.84	2219.70	-50.79	12	12	0.00	0.00	-2.86	14.80
4	4	-1758.43	65.55	-2912.02	-1811.49	13	0	0.00		-10.21	
5	0	292.22		-2346.74		13	1	0.00	0.00	-25.43	-9.78
5	1	-51.66	520.22	-2065.29	1323.32	13	2	0.00	0.00	29.25	-18.86
5	2	14.56	-383.17	1925.34	-1762.77	13	3	0.00	0.00	-71.14	17.09
5	3	36.97	353.48	-777.38	1477.53	13	4	0.00	0.00	1.95	-43.12
5	4	241.05	22.32	1661.95	-2025.08	13	5	0.00	0.00	-16.44	33.55
5	5	-263.43	-331.66	-1909.03	-2940.09	13	6	0.00	0.00	14.55	-54.10
6	0	-100.69		-2269.28		13	7	0.00	0.00	-22.86	104.53
6	1	61.04	12.06	-740.16	1624.96	13	8	0.00	0.00	5.70	-83.49
6	2	-94.53	63.35	62.25	518.82	13	9	0.00	0.00	-33.56	40.83
6	3	59.67	-44.29	790.50	1200.43	13	10	0.00	0.00	15.88	-1.62
6	4	-60.99	37.32	-330.89	988.61	13	11	0.00	0.00	7.30	-18.12
6	5	27.69	26.18	-1353.39	-800.07	13	12	0.00	0.00	-11.57	11.64
6	6	31.42	-58.62	424.12	-694.41	13	13	0.00	0.00	5.02	0.83
7	0	2.76		-168.26		14	0	0.00		-46.55	
7	1	-12.32	-21.49	21.35	-300.27	14	1	0.00	0.00	-17.53	27.65
7	2	8.86	5.46	1018.20	701.47	14	2	0.00	0.00	-30.63	-6.29
7	3	-17.05	-6.88	1135.41	637.15	14	3	0.00	0.00	-43.14	35.38
7	4	13.01	3.04	-688.69	254.00	14	4	0.00	0.00	-25.36	-25.36
7	5	-11.65	-4.86	-50.97	427.65	14	5	0.00	0.00	3.48	44.31
7	6	0.83	5.50	-692.10	-904.05	14	6	0.00	0.00	-13.00	-39.87
7	7	8.75	1.57	920.70	382.70	14	7	0.00	0.00	-1.27	69.01
8	0	2.51		212.95		14	8	0.00	0.00	-8.00	-45.04
8	1	0.48	1.82	-89.99	-489.09	14	9	0.00	0.00	-1.88	9.54
8	2	1.50	-2.79	908.86	352.13	14	10	0.00	0.00	-3.59	14.30
8	3	0.57	1.66	108.49	235.00	14	11	0.00	0.00	16.40	-16.81
8	4	-0.66	-2.41	-176.23	-57.24	14	12	0.00	0.00	-12.13	6.45
8	5	0.95	1.75	-564.44	-15.10	14	13	0.00	0.00	3.00	2.58
8	6	-0.43	-1.81	239.92	-321.08	14	14	0.00	0.00	1.18	-1.94
8	7	-0.52	0.62	-37.80	-73.72	15	0	0.00		-35.13	
8	8	0.10	1.12	317.41	204.16	15	1	0.00	0.00	-6.96	-8.82
9	0	-0.31		-248.95		15	2	0.00	0.00	-24.85	17.40
9	1	0.19	0.32	-75.71	189.91	15	3	0.00	0.00	-14.45	-9.90
9	2	-0.24	0.25	51.87	86.28	15	4	0.00	0.00	-16.04	13.07
9	3	0.34	-0.03	-96.24	330.79	15	5	0.00	0.00	21.04	0.18
9	4	-0.10	0.23	-369.89	-69.58	15	6	0.00	0.00	-15.76	-2.32
9	5	0.16	-0.23	-266.32	-217.50	15	7	0.00	0.00	15.62	17.85
9	6	-0.08	0.24	93.35	108.99	15	8	0.00	0.00	-12.45	-8.41
9	7	0.16	-0.18	120.18	-279.72	15	9	0.00	0.00	12.73	-12.22
9	8	-0.11	-0.02	-14.49	299.00	15	10	0.00	0.00	-9.72	19.80
9	9	-0.13	0.05	31.81	-105.64	15	11	0.00	0.00	14.04	-13.42
10	0	-0.02		-265.87		15	12	0.00	0.00	-7.39	2.65
10	1	-0.03	-0.06	-1.50	253.64	15	13	0.00	0.00	-0.48	2.74
10	2	-0.02	0.02	-123.98	-13.24	15	14	0.00	0.00	2.43	-1.46
10	3	-0.05	-0.01	0.56	206.48	15	15	0.00	0.00	-0.77	-0.37
10	4	0.02	0.02	-292.27	-41.34	16	0	0.00		-4.02	
10	5	-0.03	0.01	40.23	-204.70	16	1	0.00	0.00	-2.63	-60.83
10	6	0.03	0.00	-13.76	141.95	16	2	0.00	0.00	8.27	37.45
10	7	-0.03	0.01	205.04	-111.46	16	3	0.00	0.00	-4.80	-61.25
10	8	0.03	0.00	-114.74	75.81	16	4	0.00	0.00	8.29	45.31
10	9	0.00	-0.01	45.55	57.69	16	5	0.00	0.00	17.65	-43.13
10	10	-0.01	-0.01	-28.00	-82.26	16	6	0.00	0.00	-4.71	27.52
11	0	0.01		-43.30		16	7	0.00	0.00	13.05	-17.20
11	1	0.00	0.00	5.65	-4.64	16	8	0.00	0.00	-7.32	12.49
11	2	0.00	-0.01	67.61	-18.37	16	9	0.00	0.00	9.98	-20.23
11	3	0.00	0.00	-9.96	-12.32	16	10	0.00	0.00	-6.45	17.96
11	4	0.00	-0.01	-51.47	-15.99	16	11	0.00	0.00	6.30	-9.17
11	5	0.00	0.00	61.20	-161.89	16	12	0.00	0.00	-1.81	0.40
11	6	0.00	0.00	42.62	67.48	16	13	0.00	0.00	-2.99	2.20
11	7	0.00	0.00	90.44	19.19	16	14	0.00	0.00	2.74	-0.70
11	8	0.00	0.00	-34.15	-57.06	16	15	0.00	0.00	-0.61	-0.57
11	9	0.00	0.00	-35.93	95.12	16	16	0.00	0.00	-0.22	0.23
11	10	0.00	0.00	36.04	-69.43	1	0	-1.64		-0.25	
11	11	0.00	0.00	-25.12	7.02	1	1	-0.99	-0.19	0.17	0.23

The last 3 coefficients in each set define the constant external field.

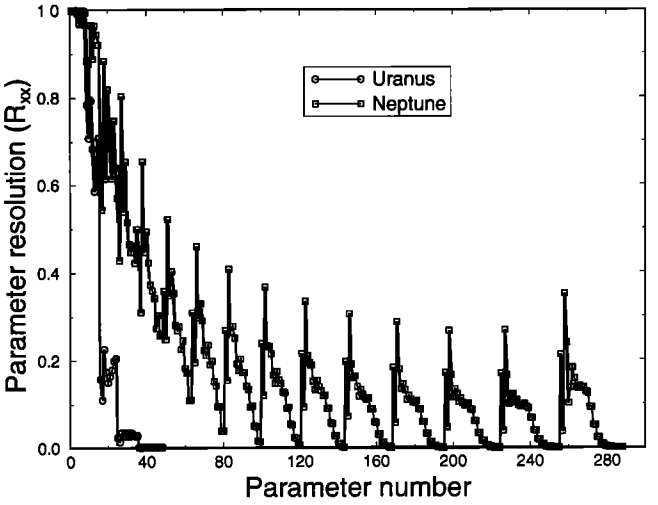

Figure 4. Resolution matrix trace elements for the models Umoh and Nmoh listed in Table 2. Parameters are ordered in increasing l and m, as $g_1^0, g_1^1, h_1^1, \ldots, g_l^0, g_l^1, h_l^1, g_l^2, \ldots, g_l^m, h_l^m, \ldots$. Values for Uranus above 49 are indistinguishable from the axis.

the planet, and fits the data. However, the numerical values of higher-degree coefficients are not individually significant, and should not be used in isolation. In particular, the larger values for the Neptune high-degree coefficients can be explained by differences in the spacecraft trajectory at the two planets, rather than any difference in field properties. We include the high-degree coefficients for Uranus to emphasize that although we performed the inversion to degree 16, these coefficients are not resolved by the data, and we have no evidence that they are nonzero.

In Figure 4 we plot the diagonal elements of the resolution matrices for both inversions. The curves are very different for the two data sets. The analysis suggests significant resolution for many of the Neptune coefficients out to degree 16, with degree 16 coefficients better resolved than degrees 11-15. This is an artefact of truncation, caused by the aliasing of higher-degree terms into the degree 16 terms, and was also noted by *Connerney et al.* [1991] in their degree 8 analysis. The aliasing does not occur with the Uranus data at any truncation level, but is observed in inversions of synthetic data sets constructed from the Neptune spacecraft trajectory with Gaussian errors (this procedure is described in more detail below), and is probably caused by the large number of data near closest approach with similar values for radius and latitude (see Figure 1). The best resolved coefficients are the h_l^1 terms, which contribute strongly to the field near closest approach. If the analysis is extended to degree and order 25, the resolution matrix elements tail off smoothly, but at the cost of a significant increase in computational complexity (the matrices are of dimension $l(l+2)$), without altering the values of the lower degree components (which are of interest). As mentioned above, the values of the high-degree coefficients are not well determined, even though they may appear well resolved.

There is considerable covariance between coefficients, particularly in the case of Neptune. For a pictorial representation of a full, nondiagonal resolution matrix, and a discussion of some of the issues involved, see *Connerney et al.* [1991].

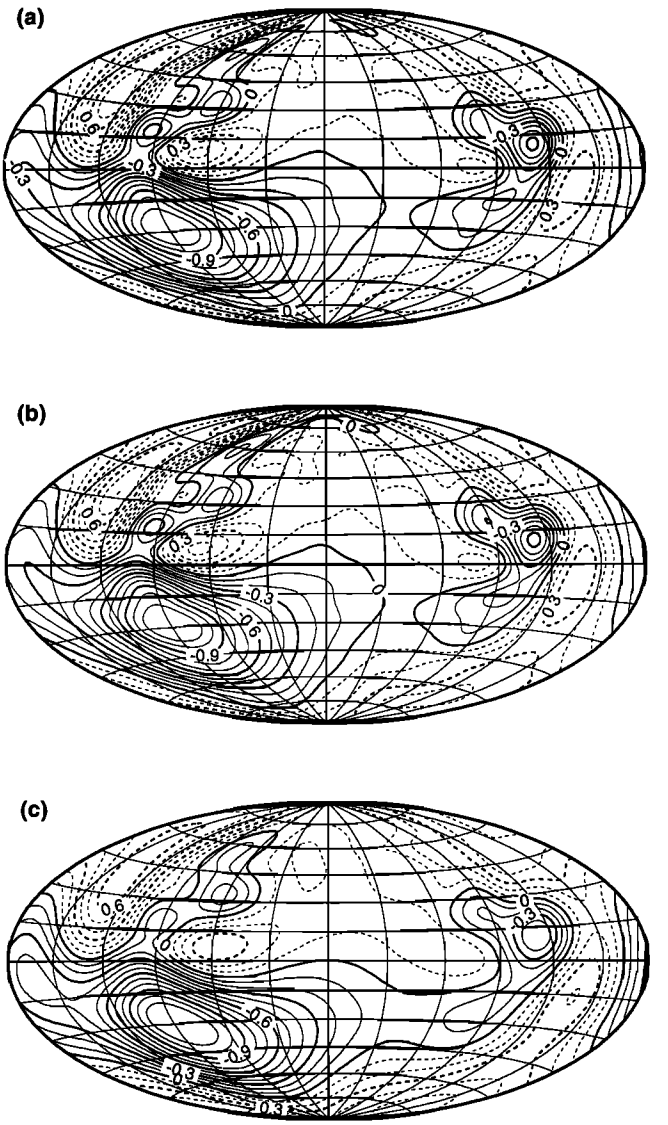

Figure 5. Maps of Neptune surface B_r for various minimized norms (see Table 1). The values for the ohmic heating norm, normalized to the observed surface heat flow, are (a) 3.12×10^{-5}, (b) 3.26×10^{-5}, (c) 1.41×10^{-5}, (d) 7.94×10^{-5}, and (e) 1.19×10^{-5}. Map (e) is of the model listed in Table 2. All maps are produced using the GMT software [*Wessel and Smith*, 1991] using a Hammer equal-area projection. Lines of latitude and longitude are separated by 15° and 30° respectively. We adopt the west longitude coordinate systems of *Connerney et al.* [1987, 1991], with zero longitude at the edge of the maps, and 180° in the center. Contour intervals are 10^{-5} nT (0.1 Gauss), and contours with negative values are dashed.

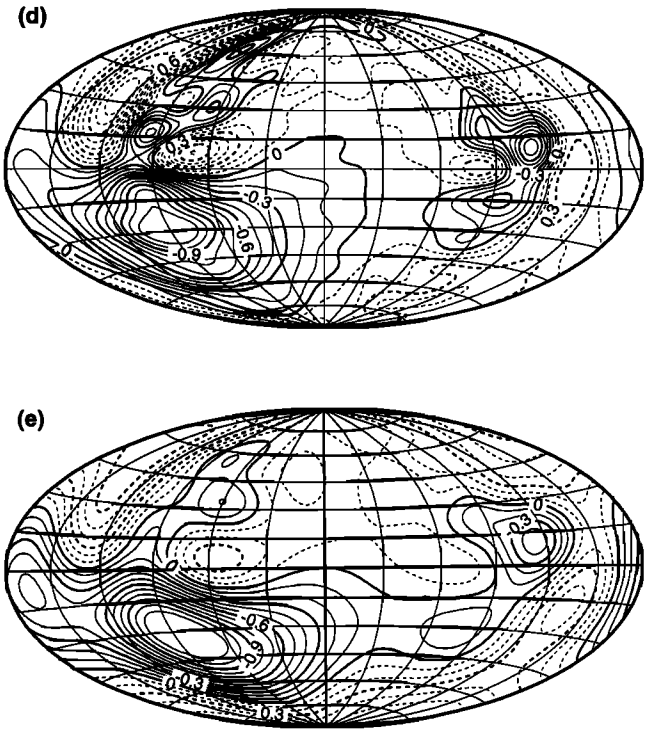

Figure 5. (continued)

Mapping the Surface Magnetic Field

To explore a range of possible models for the magnetic fields of Uranus and Neptune, we present maps of the radial field B_r calculated at the planets' surfaces. We adopt values for the surface ellipticities of 1/43.6 for Uranus [*Lindal et al.*, 1987] and 1/58.5 for Neptune [*Tyler et al.*, 1989], calculated for the 1-bar pressure surface, by convention taken as the surface of the planet. Maps derived at 1-μbar surface (the top of the atmosphere, chosen by *Connerney et al.* [1987, 1991]) are substantially similar.

In Figure 5, we show field maps of Neptune for the five norms (a) – (e). For purposes of comparison, the misfit to the data was chosen to be 0.800σ in each case. The field maps produced are broadly similar, showing that the major features are not artefacts of a particular norm but are required by the data. In their geomagnetic field modeling, *Shure et al.* [1982] sought fields which were smooth at the core-mantle boundary, but as we have discussed, the location of the equivalent region in Uranus and Neptune is not well determined. Thus for norms (a) – (d) we took $r = a$, hence seeking models which are optimally smooth at the planetary surfaces. Map (e) is calculated from the field model listed in Table 2. As can be seen from Figure 5, the main features in the field are robust to the choice of norm, essentially because convergence is dominated by the factor of $(a/r)^{2l}$ which all the norms have in common, rather than the different polynomials in l. For more quantitative comparison, as one measure of model complexity, we list in the figure caption the value in each case of the ohmic heating norm. All the models have norms within an order of magnitude of each other. For our subsequent field maps, we focus on norm (c), minimizing the horizontal derivative of the radial field, recommended by *Shure et al.* [1982] for finding a very smooth model.

Of greater significance than the particular choice of norm is the choice of damping parameter λ. In Figure 6 we present three field maps constructed for Neptune with the extreme range of λ which appears reasonable from the trade-off curve, showing that large-scale structures in the field are robust to variations in damping. However, it can also be seen that the correct choice of damping parameter is more significant than the choice

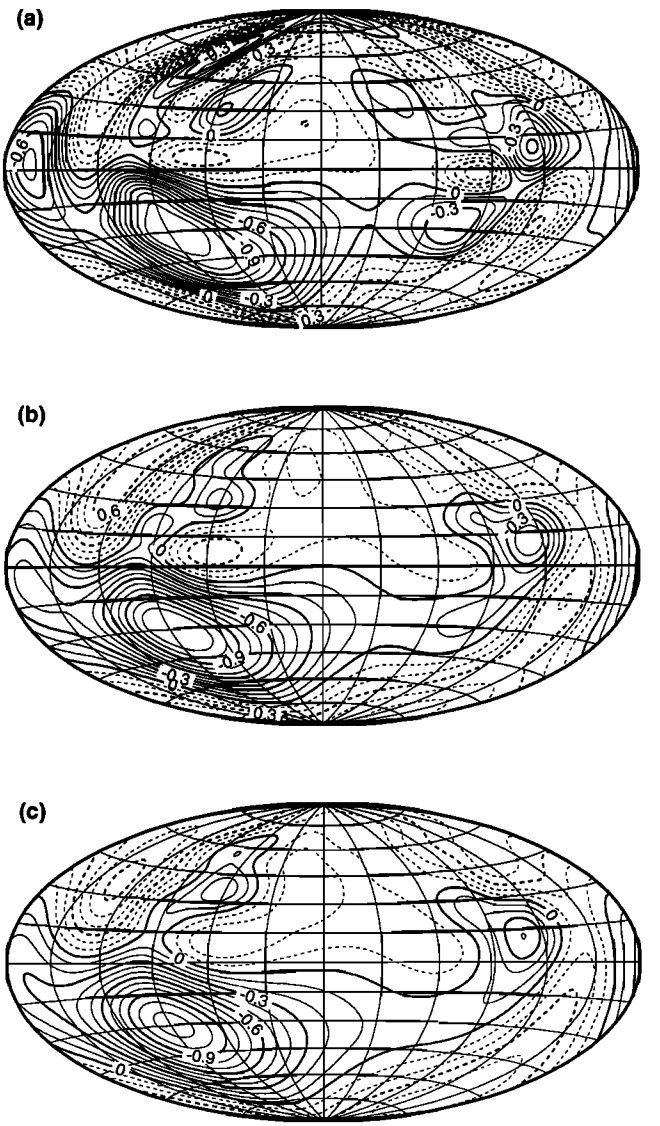

Figure 6. Neptune field models calculated using norm (c) with a range of damping parameters. (a) "Underdamped" (misfit 0.773, normalized ohmic heating norm 5.13×10^{-5}), (b) "correctly damped" (misfit 0.800, normalized ohmic heating norm 1.41×10^{-5}), (c) "overdamped" (misfit 0.984, normalized ohmic heating norm 9.40×10^{-6}).

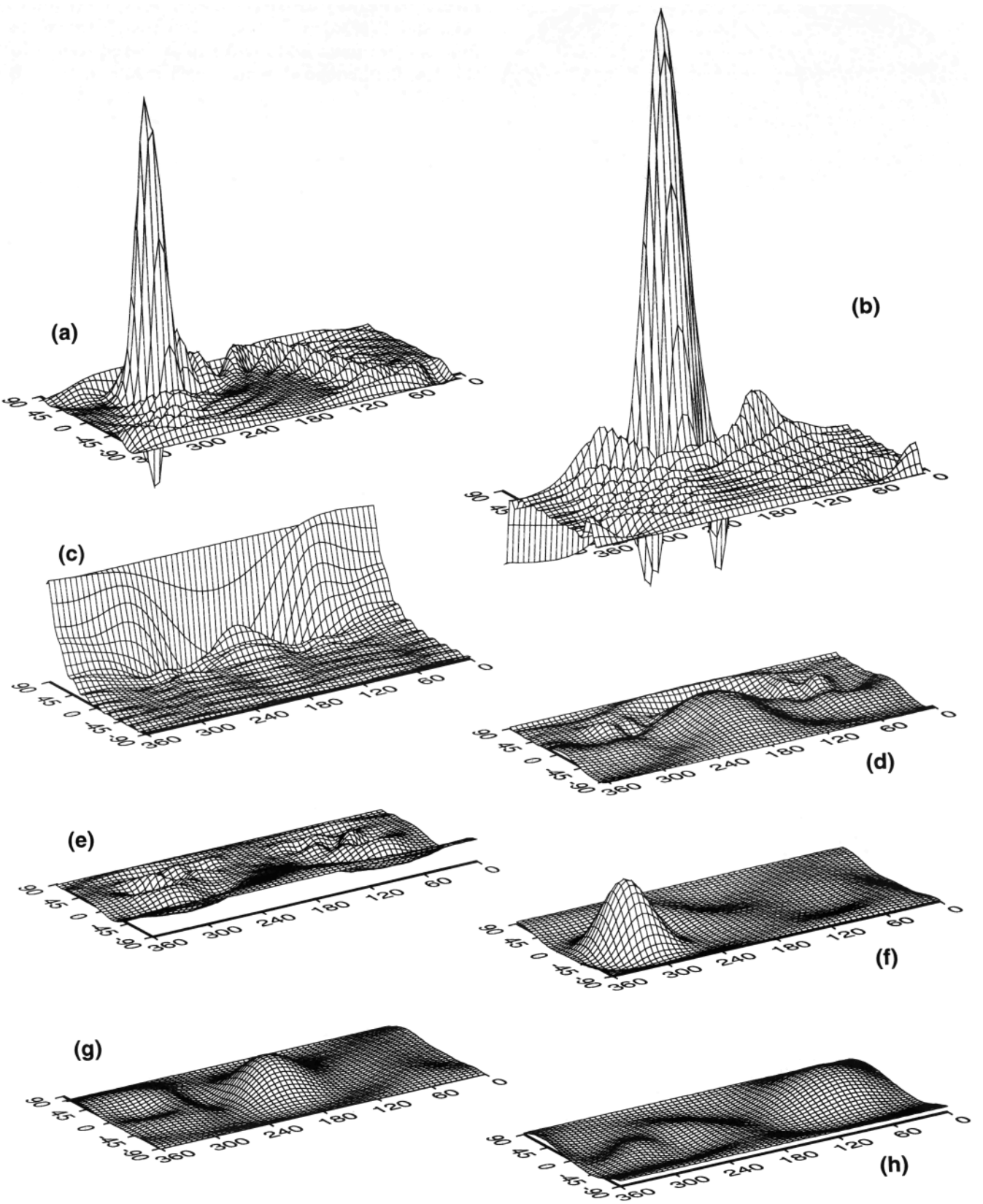

Figure 7. Averaging functions for the inversions. Neptune centered on (a) (30°N, 270°W), (b) (70°N, 180°W), (c) (70°N, 0°W), (d) (0°N, 180°W), (e) (70°S, 180°W). Uranus centered on (f) (15°S, 300°W), (g) (0°N, 180°W), (h) (30°N, 60°W).

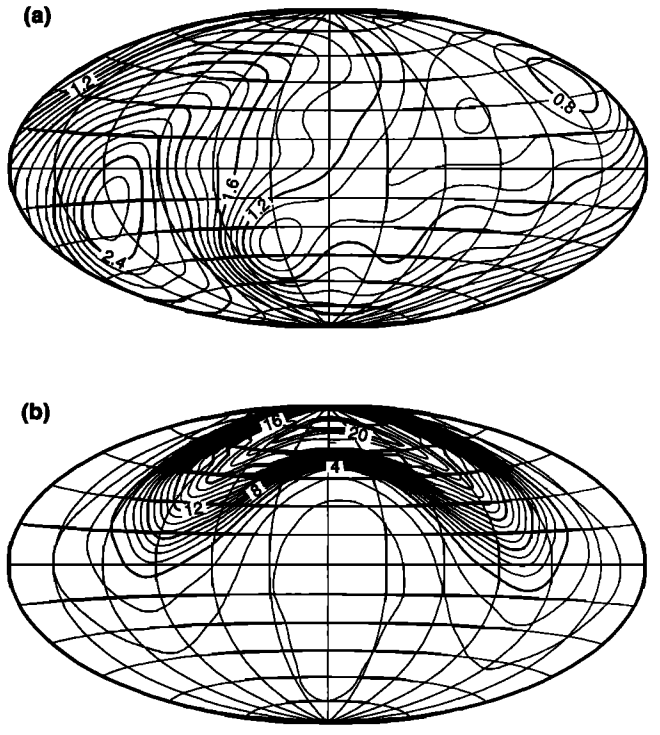

Figure 8. Peak height of averaging function for (a) Uranus and (b) Neptune.

of norm, so that detailed quantitative comparison between the different norms is of limited value.

As noted above, formal error bounds on the value of the downward continued field are either difficult to justify or excessively pessimistic [*Backus*, 1988]. An alternative approach to judging the relative confidence we can place in our maps is to calculate the averaging function, which describes the localization of a field estimate at a point. Following *Backus and Gilbert* [1967, 1968, 1970] and *Whaler and Gubbins* [1981], the expected value of the field estimate $\hat{B}_r$ is

$$\hat{B}_r(\theta_0, \phi_0) = \oint A(\theta, \phi; \theta_0, \phi_0) B_r(\theta, \phi) d\Omega \qquad (23)$$

a weighted average of the true field B_r at the planetary surface. In the absence of errors in the data, the model field is related to the true field by

$$\hat{\mathbf{m}} = \mathbf{R}\mathbf{m} \qquad (24)$$

where $\mathbf{R}$ is the resolution matrix. Using this, we may write [*Bloxham et al.*, 1989]

$$A(\theta, \phi; \theta_0, \phi_0) = \mathbf{c}^{\mathrm{T}}(\theta_0, \phi_0)\mathbf{R}\mathbf{b}(\theta, \phi) \qquad (25)$$

where $\mathbf{b}$ has elements of the form

$$(1/4\pi)(r/a)^{l+2}((2l+1)/(l+1))P_l^m(\cos\theta)\cos m\phi \qquad (26)$$

and $\mathbf{c}$ has elements of the form

$$(a/r)^{l+2}(l+1)P_l^m(\cos\theta_0)\cos m\phi_0 \qquad (27)$$

If the resolution is perfect, then $\mathbf{R}$ is an infinite dimensional identity matrix, $A(\theta, \phi; \theta_0, \phi_0)$ is a delta function, and $\hat{B}_r(\theta, \phi) = B_r(\theta, \phi)$. (To obtain a true delta function, we must add $(1/4\pi)$ to A corresponding to the $l = 0$ (monopole) term, which is known to be 0 from $\nabla.\mathbf{B} = 0$, and so perfectly resolved.) With less than perfect resolution, the averaging function has finite width. In Figure 7 we present averaging functions calculated for five locations on the surface of Neptune and three locations on the surface of Uranus. We may define a variety of different measures of "delta-ness" [*Backus and Gilbert*, 1968] to quantify how close the averaging function is to a delta function, the simplest of which is the height of the function at the sampling point, shown in Figure 8. The comparatively even data coverage for Uranus leads to a more uniform degree of localization of the surface field estimate than for Neptune, but it is also much less sharp for many locations because the data are less sensitive to higher-degree harmonics. We

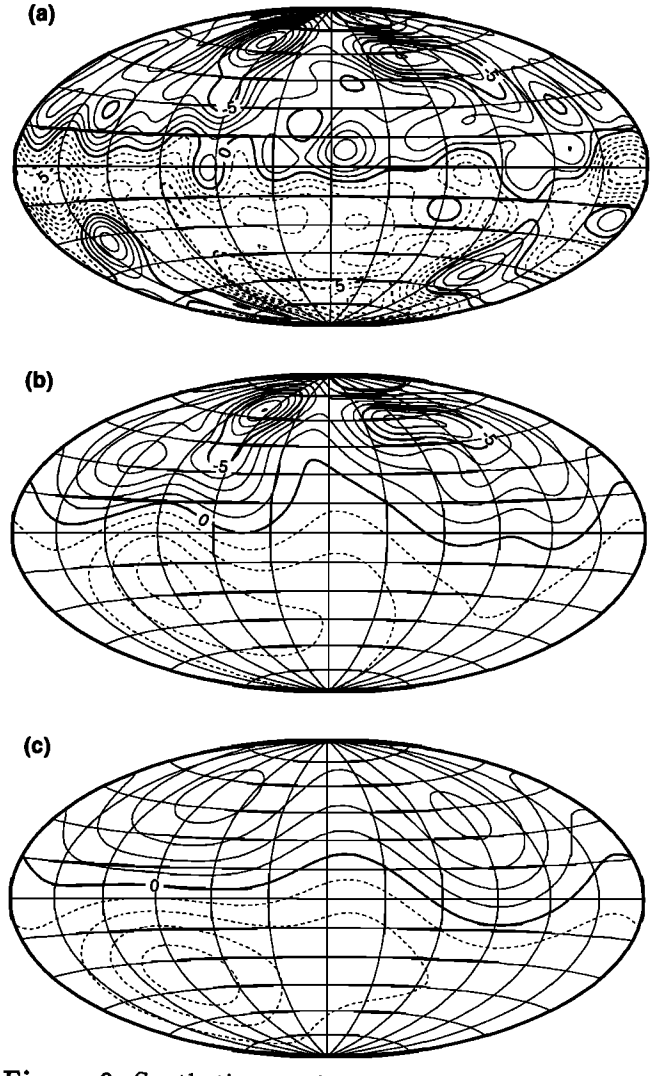

Figure 9. Synthetic experiment on the Earth's field at the CMB. (a) Original field model. (b) Minimum norm solution, using norm (c). (c) Truncated solution. Gauss coefficients for (a) and (b) are listed in Table 3.

Table 3. Magnetic Field Coefficients for 1980 Core-Mantle Boundary Model and Synthetic Solution

		Model		Synthetic				Model		Synthetic	
l	m	g_l^m	h_l^m	g_l^m	h_l^m	l	m	g_l^m	h_l^m	g_l^m	h_l^m
1	0	-183259		-177982		12	0	-3075		-509	
1	1	-11954	34236	-12856	33354	12	1	-44	315	-654	967
2	0	-22322		-30090		12	2	-1614	2069	-841	841
2	1	33814	-23782	11248	-25486	12	3	261	5384	-358	1072
2	2	18565	-2226	25757	2970	12	4	1634	-2968	340	-509
3	0	26190		31063		12	5	322	68	667	251
3	1	-44517	-6833	1005	-2264	12	6	-1038	399	-325	231
3	2	25546	5537	33233	1666	12	7	13	470	108	-168
3	3	17017	-5158	-5057	-17126	12	8	852	48	178	-522
4	0	34989		18138		12	9	-1278	-86	-167	443
4	1	29200	7907	15617	7034	12	10	-557	-2459	58	-45
4	2	14813	-9597	21463	-2966	12	11	1490	1222	21	-120
4	3	-15654	1983	-1499	5545	12	12	430	2235	-25	36
4	4	7400	-11093	16909	-2789	13	0	-346		-478	
5	0	-14850		5645		13	1	-498	-100	-283	935
5	1	24373	3167	10989	-951	13	2	648	296	-543	360
5	2	17815	10239	5957	1174	13	3	-529	2142	217	676
5	3	-5097	-10274	-3583	3169	13	4	-173	-359	333	-677
5	4	-11066	-5305	3935	-2357	13	5	1818	-244	560	191
5	5	-3285	6279	1754	3104	13	6	-249	148	-237	-84
6	0	5934		6743		13	7	456	1213	3	-46
6	1	8203	-1903	4669	-8094	13	8	-977	114	184	-391
6	2	5231	11599	4455	1266	13	9	-14	1038	-159	282
6	3	-23923	8792	-6057	1549	13	10	-137	455	11	57
6	4	407	-5405	777	-5759	13	11	326	-276	54	-143
6	5	1721	-318	760	4183	13	12	134	176	-35	37
6	6	-13434	2154	-2325	-2047	13	13	697	-235	0	14
7	0	16449		7803		14	0	9		-303	
7	1	-13596	-18681	1214	-9924	14	1	278	45	-54	537
7	2	410	-6175	4803	419	14	2	9	-304	-251	85
7	3	4671	-1089	-5708	1119	14	3	-17	-186	440	242
7	4	-2782	3707	1267	-6248	14	4	-168	285	266	-644
7	5	201	4118	300	3546	14	5	387	0	360	90
7	6	2442	-5286	-758	-931	14	6	-157	402	-198	-128
7	7	-381	-2382	-533	-892	14	7	187	163	-82	-31
8	0	7668		5947		14	8	-192	380	152	-202
8	1	2894	2795	-594	-8175	14	9	48	-97	-126	145
8	2	-185	-7581	3244	807	14	10	224	159	-28	111
8	3	-4357	1785	-4795	709	14	11	155	-150	70	-134
8	4	-2826	-9246	1368	-3854	14	12	-119	216	-32	22
8	5	1933	3784	201	1676	14	13	242	-80	-8	26
8	6	1187	6644	-257	1178	14	14	409	180	7	-6
8	7	2460	-5304	-163	-1767	15	0	29		-140	
8	8	-771	-6010	124	765	15	1	53	25	48	145
9	0	4010		3204		15	2	-125	3	-65	-15
9	1	7623	-15940	-1399	-4992	15	3	43	-41	432	-64
9	2	1309	11959	1130	1580	15	4	6	54	159	-477
9	3	-9333	6507	-3784	660	15	5	-2	-32	149	23
9	4	6956	-3729	904	-1426	15	6	-55	2	-172	-48
9	5	-2598	-4738	245	403	15	7	-117	11	-128	-42
9	6	-880	7015	-412	2094	15	8	52	-46	121	-44
9	7	5071	7291	129	-1742	15	9	18	-89	-86	55
9	8	1040	-4562	-47	503	15	10	-56	-100	-43	118
9	9	-4299	1607	100	260	15	11	88	-3	73	-107
10	0	-4665		1062		15	12	46	-41	-20	2
10	1	-5378	1979	-1461	-1921	15	13	14	-38	-16	33
10	2	3278	711	-324	1798	15	14	18	-69	11	-7
10	3	-7403	2994	-2562	972	15	15	14	58	0	-3
10	4	-2724	7730	495	-316	16	0	-2		-35	
10	5	5509	-6131	428	89	16	1	27	-8	69	-85
10	6	4222	-511	-527	1725	16	2	-17	-11	21	-17
10	7	1175	-2147	224	-1127	16	3	15	2	317	-200
10	8	2708	4635	-23	-66	16	4	-2	-5	61	-275
10	9	3758	-1036	-23	501	16	5	-59	-12	-16	3
10	10	95	-8603	53	-182	16	6	-2	-4	-131	49
11	0	5664		-111		16	7	-9	-36	-135	-52
11	1	-2138	1241	-1108	130	16	8	15	5	108	51
11	2	-3707	3589	-890	1424	16	9	4	2	-49	3
11	3	4566	-2674	-1326	1199	16	10	-1	-30	-42	95
11	4	546	-6239	344	-244	16	11	8	6	65	-75
11	5	-2282	1864	615	187	16	12	-9	6	-7	-13
11	6	-703	-662	-456	895	16	13	-22	-36	-22	34
11	7	3331	-4967	196	-515	16	14	-26	-16	12	-6
11	8	3631	-986	98	-449	16	15	28	5	2	-5
11	9	-129	-3209	-128	552	16	16	34	3	-2	1
11	10	3961	-2595	82	-153	1	0	0.00		1.44	
11	11	6533	1864	-12	-65	1	1	0.00	0.00	0.30	-0.04

The last 3 coefficients in each set define the constant external field.

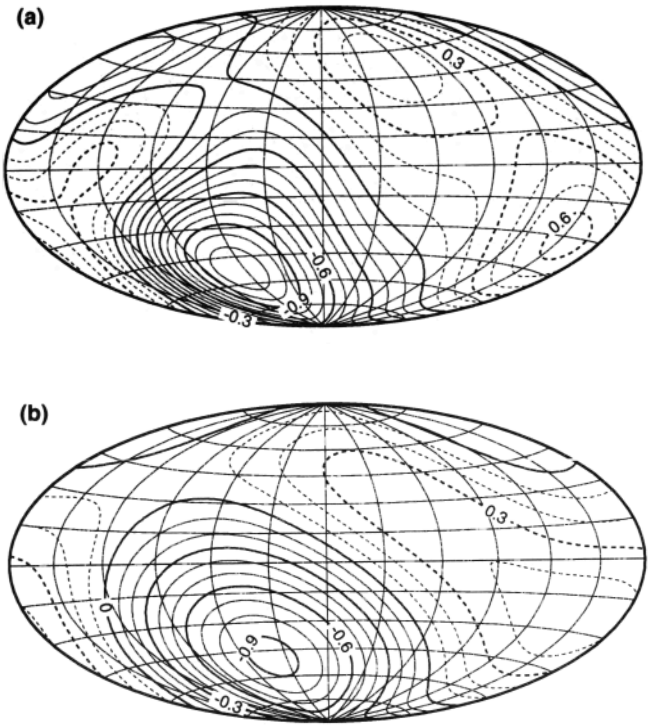

Figure 10. A comparison of (a) minimum norm and (b) truncated SVD solutions for the surface radial field of Uranus. Field strength in Gauss (10^{-4} T).

are unable to compare different areas of our maps of the surface field of Neptune, or features on Uranus and Neptune, as differences are far more sensitive to data coverage than field morphology.

To further explore these issues, we perform an experiment to examine how well we can recover a known field model with data of similar quality to those obtained at Neptune. We form a synthetic by using a known magnetic field model to calculate the components of magnetic field at a set of points in space corresponding to the coordinates of the Neptune data. We do this using the 1980 geomagnetic main field model of *Gubbins and Bloxham* [1985]. However, because the surface geomagnetic field is dominated by the axial dipole term g_1^0, in order to better mimic the complex morphology observed at Uranus and Neptune, we map the core-mantle boundary field to the surface of the planet. We then add Gaussian errors to the synthetic data in proportion to the postulated errors at Neptune, and seek a smooth field model that fits the data to 1.0σ. The effect of this is to produce a data set that approximates that which would have been collected by Voyager with a Neptune-like fly-by of Earth's core.

In Figure 9, we show maps of the 1980 model geomagnetic field at the core-mantle boundary, a minimum norm solution for the field, obtained from the synthesized data with the Neptune trajectory, and a truncated solution, equivalent to a truncated SVD solution. The minimum norm solution clearly does a much better job of modeling the field in the northern hemisphere. As we would expect from our analysis of the averaging function, the map has the most structure where there is maximum data resolution, and does not alias in field structure where the data provide no information. The 1980 field model has a similar amount of structure in the northern and southern hemispheres, but this is clearly not true for the minimum norm solution, which confirms that we must take great care in interpreting field structure of any model we produce. Both the original geomagnetic model and the minimum norm solution fit the data to about 1σ (0.989σ for the initial model, and 0.999σ for the minimum norm solution), but the value of the norm (the roughness) for the original geomagnetic model is 4 times larger than that for the minimum norm solution.

In Table 3, we present the Gauss coefficients for the 1980 field model and the minimum norm solution, scaled to be valid at the core-mantle boundary. Comparison of the two sets of coefficients provides some idea of how much credence to place in individual coefficients of our model Nmoh. The external field coefficients, listed at the end of the table, are of comparable magnitude to those obtained from the Uranus and Neptune

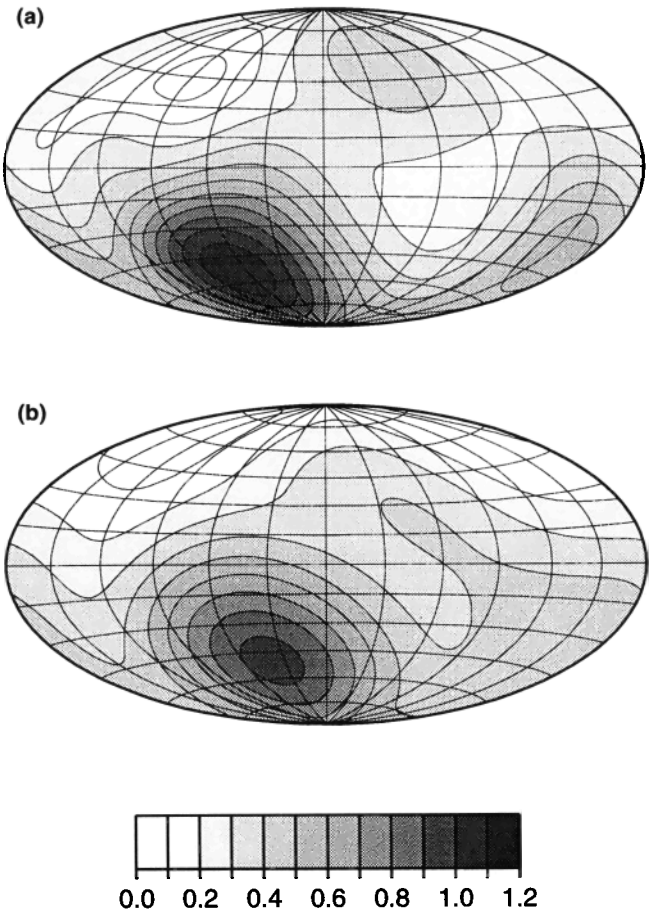

Figure 11. A comparison of (a) minimum norm and (b) truncated SVD solutions for the surface magnetic field intensity of Uranus. Field strength in Gauss (10^{-4} T).

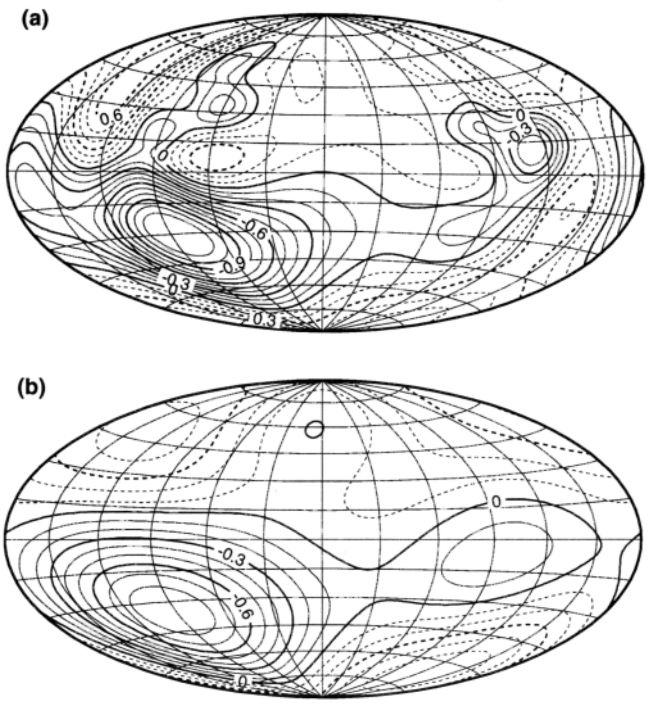

Figure 12. A comparison of (a) minimum norm and (b) truncated SVD solutions for the surface radial field of Neptune. Field strength in Gauss (10^{-4} T).

data, despite there being no external field components in the 1980 field model. If we change the magnitude of the error added to our synthesized data, the external field estimates change in proportion, so we cannot assign any meaning to the derived external coefficients.

In Figures 10-13, we present candidate field models for the surface radial field and total intensity of Uranus and Neptune. To compare our results with previous work, we also show maps derived from the Q_3 model for Uranus [*Connerney et al.*, 1987] and the O_8 model for Neptune [*Connerney et al.*, 1991]. Encouragingly, the previous models are almost indistinguishable from our models if the latter are truncated to the same degree (degree 2 for Uranus and degree 3 for Neptune). The minimum norm solution and truncated SVD solution are similar for Uranus, but not for Neptune, reflecting the difference in sampling resolution and data coverage. For Neptune, the SVD solution masks features in the field that are reproducibly present for the various norms, and for a range of damping parameters.

Clearly, it would be unwise to claim that our maps provide a good representation of the surface fields of Uranus and Neptune. In particular, the field of Neptune is likely to be considerably more detailed in the southern hemisphere than our maps imply. However, our maps have several advantages over the previous maps determined using SVD. First, they do not suppress structure required by the data in one region simply because resolution of another region is less good. Second, the maps are the smoothest possible for a given fit to the data, the form of smoothness being defined by the particular norm used, which provides a lower bound on the field complexity lacking from the maps of truncated models. Third, unlike the truncated models Q_3 and O_8, our models can provide meaningful field estimates away from the spacecraft trajectory and still fit the data.

In the framework of the caveats described above, what can be concluded from the field maps? Clearly, the surface field of Neptune is highly complex. The strongest feature at the surface is the dominant southern hemisphere field maximum near 30°S, 270°W, previously identified as the southern magnetic pole. This is also resolved by the truncated models (albeit at a lower intensity), as it is a strong, long wavelength, feature. There seems to be no comparably strong feature in the northern hemisphere. This is not an artefact of poor data coverage, as the best resolution is obtained in high northern latitudes, as can be seen from Figure 8. Other smaller robust features include a local maximum in B_r at 10°S, 70°W, and large but less sharp minima in B_r located near and over the north and south geographical poles.

The fact that the field is well determined in high latitudes could have important implications for the study

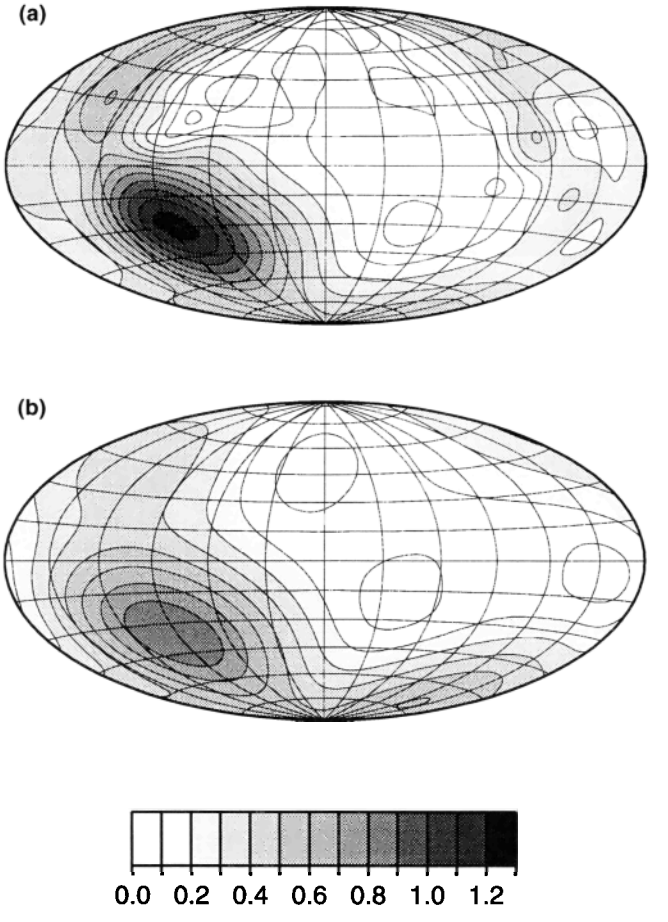

Figure 13. A comparison of (a) minimum norm and (b) truncated SVD solutions for the surface magnetic field intensity of Neptune. Field strength in Gauss (10^{-4} T).

of radio sources. For example, *Ladreiter et al.* [1991], using an offset tilted dipole model of the magnetic field [*Ness et al.*, 1989], modeled the smooth kilometric radiation from Neptune as being from two sources. One of these was well localized near the southern magnetic pole, but the other location was poorly determined because of poor resolution of the field model within $3R_N$, and could have occupied a band of up to 120° longitude. We are able to provide a considerably improved estimate of the field structure in this region, which could result in better understanding of the origin of the radio emissions, although we emphasize that this must come from direct modeling using the data, not from using our field maps or models.

Spectral Analysis

The power spectrum provides an alternative means for examining a field model. The most common choice of power spectrum is the mean square field intensity, first used by *Mauersberger* [1956] and *Lowes* [1974] and given by

$$P(l,r) = (l+1)\,(a/r)^{2l+4} \sum_{m=0}^{l} [(g_l^m)^2 + (h_l^m)^2] \quad (28)$$

Other choices include the stored magnetostatic energy (norm (d) from Table 1) [*Benton and Alldredge*, 1987].

For the geomagnetic field, if r is chosen to be the radius of the core, the power up to degree $l = 14$ is approximately white (higher l being assumed dominated by lithospheric field sources) [e.g., *Langel and Estes*, 1982]. It has been speculated that if the same procedure is applied to non-Earth fields, and a depth can be found at which the spectrum is close to white, this depth could be related to the source region for the field. Application to the fields of Jupiter and Saturn is encouraging, giving depths ($0.8R_J$ and $0.4R_S$) consistent with theoretical [*Stevenson*, 1982] and experimental [*Mao and Hemley*, 1989] estimates of the pressure at which hydrogen changes phase from a molecular to a highly conducting metallic form. However, with model resolution only to degree 3, this conclusion must be regarded with some caution, especially given that for the Earth the dipole and quadrupole terms fit the calculated spectrum poorly. The fit of low-degree terms to the geomagnetic spectrum is improved if axial coefficients are excluded [*Schulz and Paulikas*, 1990], but this procedure is not applicable to the field of Saturn, for which the best field models are axially symmetric [*Connerney et al.*, 1982; *Davis and Smith*, 1990].

In Figure 14 we plot the spectra for our preferred field models (Table 2). Above degree 3, the spectra are dominated by the smoothing that we have imposed on our inversions, so we limit our attention to the first three degrees only. Then, we obtain depths for white spectra of 1.05 for Neptune and 0.84 for Uranus. This suggests that it is not possible to use the power spectrum as a tool for determining the extent of the dynamo region

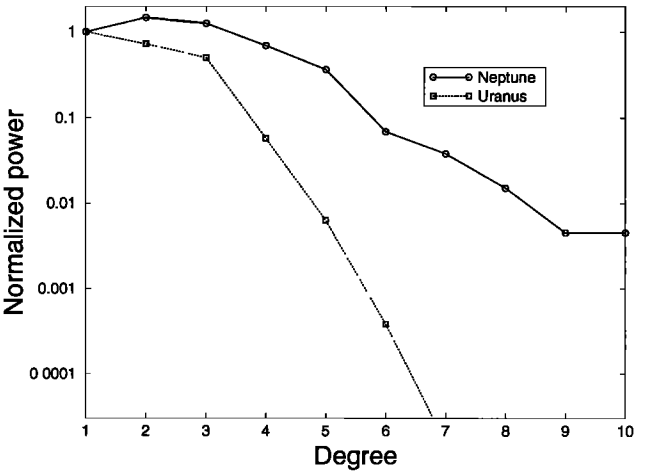

Figure 14. Magnetic spectra for the surface fields of Uranus and Neptune. Power in each degree normalized to dipole power.

for Uranus and Neptune. *Schulz and Paulikas* [1990] have suggested normalizing each value by $1/(2l+1)$, the number of modes in each degree, in which case the altered spectrum does fall off with degree at $r = a$, but neither theoretical considerations nor the geomagnetic spectrum supports such an approach.

Discussion

Extremal Modeling: Dipole Fit

Whilst we are unable to choose between many similar models for the planetary magnetic fields on the basis of the heat flow constraint, we may reject more extreme models by direct hypothesis testing against the data. As an example, we consider the hypothesis that the unusual dipole tilts are not real but instead are an artefact of poor data coverage, which we may test by seeking fields with a particular dipole tilt θ_0. If we write the axial dipole coefficient in terms of the equatorial dipole terms and the dipole tilt

$$g_1^0 = \cot\theta_0 \sqrt{(g_1^1)^2 + (h_1^1)^2} \quad (29)$$

the number of free parameters is reduced by 1. However, the field now depends nonlinearly on g_1^1 and h_1^1, requiring adoption of an iterative scheme to search for a field model [*Gubbins and Bloxham*, 1985]. Instead, we write condition (29)

$$(g_1^1)^2 + (h_1^1)^2 - \tan^2\theta_0 (g_1^0)^2 = 0 \quad (30)$$

which is in the form of a quadratic norm, and can be incorporated with ease into the linear inversion. The function to minimize (analogous to equation (11)) becomes

$$(\boldsymbol{\gamma} - \mathbf{Am})^{\mathrm{T}} \mathbf{C_e}^{-1} (\boldsymbol{\gamma} - \mathbf{Am}) + \lambda \mathbf{m}^{\mathrm{T}} \boldsymbol{\Lambda} \mathbf{m} + \mu \mathbf{m}^{\mathrm{T}} \boldsymbol{\Gamma} \mathbf{m} \quad (31)$$

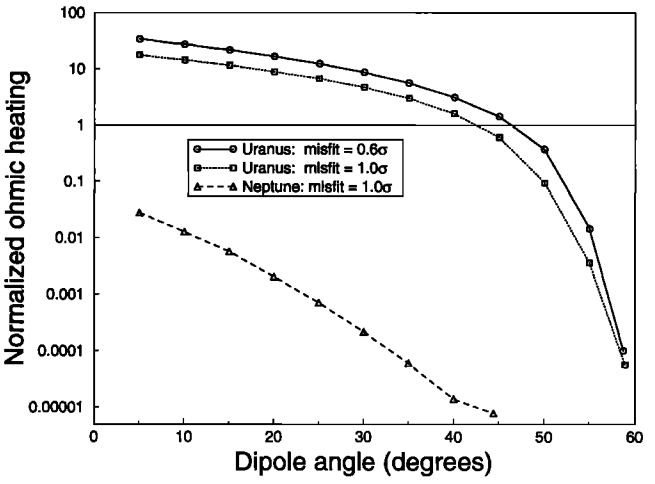

Figure 15. Ohmic heating bounds for forced dipole solutions for Uranus and Neptune. In each case the point furthest to the right allows free determination of the dipole terms. Misfits are given in terms of original nominal misfits (our preferred models Umoh and Nmoh have misfits of 0.6σ and 0.8σ, respectively.) Ohmic heating normalized to observed surface heat flow.

where the matrix Γ has elements $-\tan^2(\theta_0)$, 1 and 1 in its first three leading diagonal positions and zeros elsewhere. We proceed by varying the damping parameters λ and μ so as simultaneously to satisfy equation (30) and obtain an adequate fit to the data.

In Figure 15, we plot the heat flow (normalized to the surface heat flow) against imposed dipole tilt for minimum ohmic heating norm solutions. For Uranus we seek solutions with misfits to the data of 0.6σ or 1.0σ, and for Neptune of 1.0σ. If we believe that the poloidal field ohmic heating should be at most no greater than the surface heat flow (a relatively weak assumption), then we must conclude that the dipole tilt of Uranus can be no less than about 46° if we require to fit the data to 0.6σ (0.3 nT), and no less than 42° if we allow a misfit of 1.0σ (0.5 nT). As the curve in Figure 15 is steep, this result is robust to significant changes in conductivity structure. Reducing the dipole tilt by only 5° from the unconstrained value increases the magnitude of the ohmic heating by 2 orders of magnitude. We could avoid this by allowing a much worse fit to the data, but this would seem unjustified, given the existence of simple smoothed models which do fit the data well. In fact, our conclusion could be strengthened, as for the purposes of internal field modeling, we have ignored data from more than $8.0R_U$ as being excessively contaminated by external fields. While these data have a low signal-to-noise ratio, they still place a strong constraint on the possible dipole orientation.

For several reasons, we are unable to arrive at such a firm conclusion for Neptune. First, the observed surface heat flow from Neptune is 10 times greater than that from Uranus. Second, the dipole terms are less well resolved by the Neptune data than the Uranus data, allowing the dipole coefficients to be reduced by including combinations of poorly constrained eigenvectors from the null space. Third, the dipole terms are weaker relative to higher-degree terms, and so contribute comparatively less to the ohmic heating bound.

Extremal Modeling: Power Spectra

We may also use extremal modeling to strengthen the basis of our spectral arguments. We explore whether it is possible to obtain a Neptune field model with a white power spectrum at the planet's surface by seeking a field such that the quadrupole power equals the dipole power. In other words, we require

$$2\sum_{m=0}^{1}\left((g_1^m)^2+(h_1^m)^2\right)=3\sum_{m=0}^{2}\left((g_2^m)^2+(h_2^m)^2\right) \quad (32)$$

Once again, this constraint can easily be incorporated into equation (11)) as a quadratic norm, so again the inversion remains linear. In Figure 16 we show the results for a model with a 1.0σ misfit to the data, and a normalized heat flow bound of 1.05×10^{-4}, 10 times larger than an unconstrained model. As a consequence of the damping, the power in the octupole and higher-degree terms is increased above that of the dipole. If these degrees in turn are more heavily damped, then power is forced to higher harmonics still, and the ohmic heating bound rapidly approaches the value of the surface heat flow. Thus we may conclude that it is not possible to find a field model for Neptune which fits the data and has a white spectrum at or below the surface of the planet.

Symmetry

Rädler and Ness [1990] have explored the symmetry properties of planetary magnetic fields using calculated field models, quantifying the departure from axisymmetry by calculating the fraction of the power in nonaxial

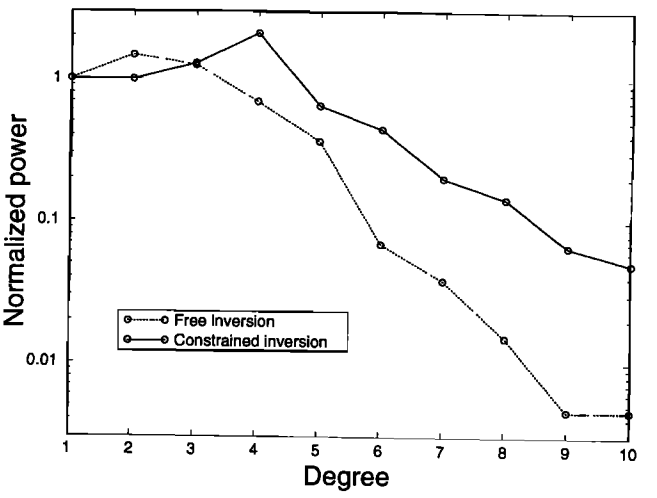

Figure 16. Magnetic spectrum for Neptune with equal dipolar and quadrupolar power. Misfit to data 1.0σ, ohmic heating bound 10 times optimal value.

Table 4. Table of Symmetry Parameters

Planet	Parameter	θ_a	ϕ_a	Value
Uranus	$\hat{f}_1$	58.8	306.1	0.00
	$\hat{f}_2$	38.8	330.6	0.03
	$\hat{f}_3$	58.0	7.3	0.28
	$\hat{f}(r/a = 10)$	58.5	306.2	0.04
	$\hat{f}(r/a = 1)$	43.0	312.4	0.29
	$\hat{f}(r/a = 0.8)$	38.2	300.3	0.40
	$\hat{f}(r/a = 0.5)$	53.5	3.7	0.57
Neptune	$\hat{f}_1$	45.6	288.8	0.00
	$\hat{f}_2$	64.8	269.1	0.25
	$\hat{f}_3$	20.3	155.0	0.01
	$\hat{f}(r/a = 10)$	46.1	288.4	0.01
	$\hat{f}(r/a = 1)$	56.5	276.0	0.48
	$\hat{f}(r/a = 0.8)$	24.0	136.9	0.61
	$\hat{f}(r/a = 0.5)$	19.7	249.8	0.62

components. They use equation (8) to define the power at degree l and order m as

$$e_l^m = (l+1)\left(\frac{a}{r}\right)^{2l+4}\left((g_l^m)^2 + (h_l^m)^2\right) \quad (33)$$

They further define the power in a particular degree $e_l = \sum_m e_l^m$, axial power $e^0 = \sum_l e_l^0$, and total power $e = \sum_{l,m} e_l^m$, and construct a symmetry parameter

$$f = \frac{e - e^0}{e} \quad (34)$$

which is zero for a field axisymmetric about the rotation axis, and 1 if all axial components are zero. The symmetry parameter f is clearly a function of radius. The only physically sensible value of r to consider is the radius of the conducting region within the planet, as at lesser radii, representation of the field as the gradient of a scalar is invalid, whilst at greater radii, low-degree terms will dominate. However, except for the Earth, the boundaries of the conducting regions in the planets are not well defined, so a range of possible r must be investigated. To consider the symmetry of a particular degree, independent of radius, we consider

$$f_l = \frac{e_l - e_l^0}{e_l} \quad (35)$$

Rädler and Ness [1990] examine the fields of Earth, Jupiter, and Saturn and find a high degree of axisymmetry about the rotation axis, particularly for Saturn, as well as a high degree of antisymmetry about the equatorial plane. They observe that the field of Uranus is far from axially symmetric but does exhibit strong symmetry about an alternative axis. The coefficients of *Connerney et al.* [1987] are restricted to $l = 2$, so their conclusion is limited, and follows because the quadrupole term displays significant symmetry about an axis close to the dipole axis. However, if this conclusion could be demonstrated more generally, for higher-degree terms in the spherical harmonic expansion, it would have profound implications for the study of dynamo theory. No data for Neptune were available at the time of their study.

Clearly, the fields of Uranus and Neptune are not strongly axisymmetric about the rotation axes, as can be seen from the large (and robust) values of their dipole tilts. However, following *Rädler and Ness* [1990], we wish to consider other possible axes of symmetry, for which an appropriate symmetry parameter is

$$\hat{f} = \frac{e - \hat{e}^0}{e} \quad (36)$$

where $\hat{e}^0$ is calculated from a rotated set of the coefficients $\hat{g}_l^0$. For a particular axis (θ_a, ϕ_a), these coefficients are written

$$\hat{g}_l^0 = \sum_{m=0}^{l} P_l^m(\cos\theta_a)(g_l^m \cos m\phi_a + h_l^m \sin m\phi_a) \quad (37)$$

This differs from equation (11) of *Rädler and Ness* [1990] by a factor of $\sqrt{4\pi}$ due to our use of conventionally Schmidt-normalized spherical harmonics, as per equation (2) [*Langel*, 1987].

We examine the symmetry properties of the coefficient sets listed in Table 2. Our results are summarized in Table 4, and agree with the analysis of *Rädler and Ness* [1990] for Uranus. However, when we include higher-degree coefficients, we do not observe strong symmetry in the total field (measured by $\hat{f}$) for any reasonable r. The Neptune field model does not demonstrate any strong symmetry. In particular, we show in Appendix B that the value of $\hat{f}_2 = 0.25$ is the maximum possible value, and thus the quadrupole field is of the form which is least well suited to representation by an axial field.

Extremal Modeling: Symmetry

The discussion of symmetry properties is limited by poorly determined high-degree Gauss coefficients. However, we can make more general statements using extremal modeling. We adapt the formalism used for examining the dipole orientation, choose a particular axis (θ_a, ϕ_a), and look for fields with a defined value of $\hat{f}$. Note that in this case the damping matrix is not diagonal. More generally, we could attempt to find the most

Table 5. Results for Optimal Symmetry, $\hat{f} = 0.05$, Misfit $= 1.0\sigma$

	r/a	θ_a	ϕ_a	H/Q_S	H/W_{opt}
Uranus	1.0	43.0	312.4	3.0×10^{-4}	3.2
Neptune	1.0	56.5	276.0	1.7×10^{-3}	17.4
Uranus	0.75	37.0	296.2	4.0×10^{-4}	4.2
Neptune	0.8	53.5	278.0	1.7×10^{-4}	1.8

symmetric field possible for given misfit to the data and ohmic heating by directly inverting for (θ_a, ϕ_a) along with the field coefficients, but this would make the inversion nonlinear. Here we present results for the optimal axes calculated with the field coefficients above. We consider both symmetry at the surface ($r = a$) and also at a depth characteristic of the dynamo region ($r/a = 0.75$ for Uranus and $r/a = 0.8$ for Neptune), although our conclusions are not sensitive to the particular values of r/a. We look for fields with a misfit of 1.0σ, and use the calculated ohmic heating bound as a measure of how reasonable the field model is. The results are presented in Table 5. Q_S is the measured surface heat flow, and W_{opt} is the ohmic heating bound of the optimal models Umoh and Nmoh. For both planets it is possible to construct fields with a high degree of symmetry about the chosen axis. However, it is equally possible to construct fields with a similar misfit and ohmic heating norm, but with poor axial symmetry. We conclude that there is insufficient evidence to suggest that the fields display significant symmetry about a particular axis, particularly in the case of Neptune. However, equally, the data do not preclude such fields.

Our results indicate some of the risks of hypothesis testing with poorly determined Gauss coefficients. As can be seen from both the synthetic experiments and the extremal modeling, while certain physical properties of the fields are robust to different models, the values of the Gauss coefficients which make up those models are not. Instead, tests should be made directly against the data. The data are available from NSSDC, and the models described in this paper can be calculated straightforwardly.

Conclusions

In this paper, we have presented and analyzed field models for Uranus and Neptune, broadly confirming the results of earlier workers. In the absence of new data, further insight must come from other magnetic related observations. We have already mentioned the possibility of using our Neptune model to study the northern hemisphere radio sources. Using the footprint location of the Io flux tube to constrain the field of Jupiter has been considered [*Connerney*, 1992; *Connerney et al.*, 1993], and similar studies may be possible for Uranus and Neptune. However, such considerations are outside the scope of this paper.

We conclude by considering the still open question of why these two fields should be so different from those of the other planets. Previous workers have sought to explain this in a variety of ways, including internal convection with a few large-scale cells [*Connerney et al.*, 1987, 1991], a thin-shell dynamo [*Ruzmaikin and Starchenko*, 1991], magnetic field reversal [*Schulz and Paulikas*, 1990], and the unusual orbital obliquity of Uranus [*Podolak et al.*, 1991], although none of these mechanisms is entirely convincing. Here we examine two separate ways in which Uranus and Neptune are significantly different from the other planets, and how these might affect the dynamo process.

First, we consider the dynamical balances that operate in planetary dynamos. As we have mentioned, measurements of the magnetic field only provide information about the poloidal ingredient of the magnetic field. The toroidal field is unknown and, according to some dynamical arguments, may be significantly larger than the poloidal field. It is usually assumed that planetary dynamos, including those of Uranus and Neptune [*Hide*, 1988; *Podolak et al.*, 1991], operate in magnetostrophic balance. This is a dynamical assumption that the Lorentz and Coriolis forces are of similar magnitude, so that

$$2\rho\mathbf{\Omega} \wedge \mathbf{u} \sim \frac{1}{\mu_0}(\nabla \wedge \mathbf{B}) \wedge \mathbf{B} \tag{38}$$

where ρ is the density of the dynamo region, $\mathbf{\Omega}$ is the angular rotation frequency of the planet, and μ_0 is the permeability of free space. In the case of the Earth, we use the poloidal field at the core-mantle boundary (estimated using equation (8)) as a measure of the poloidal field strength in the core, and find that this is too weak to balance the Coriolis force. Thus, the balance must be fulfilled by the toroidal field. Following the treatment of *Hide and Roberts* [1979], this gives

$$B_T \sim \sqrt{2\Omega\rho\mu_0 UL} \tag{39}$$

where U and L are characteristic velocity and length scales. For the Earth it is possible to estimate U from models of the flow at the core-mantle boundary [*Bloxham and Jackson*, 1991].

Such estimates are not available for Uranus and Neptune, so instead we adopt an indirect approach to estimate B_T. We define the magnetic Reynolds number $R_m = \mu_0\sigma UL$, in which case equation (39) gives

$$B_T \sim B_s(R_m)^{\frac{1}{2}} \tag{40}$$

where the scale field is defined $B_s = \sqrt{2\Omega\rho/\sigma}$. We

further assume that in the magnetostrophic regime the toroidal field is produced by differential shear of the poloidal field (the so-called ω-effect), so that

$$B_T \sim R_m B_P \tag{41}$$

where the magnetic Reynolds number is based on length and velocity scales characteristic of the shear. If the two magnetic Reynolds numbers (one based on the main flow, the other on the shear) are similar, this in turn suggests

$$B_P = B_s(R_m)^{-\frac{1}{2}} \qquad B_T B_P = {B_s}^2 \tag{42}$$

For the Earth, the indirect estimate of the toroidal field obtained from equation (42) agrees well with the direct estimate from equation (39). Note that both of these estimates are based on dynamical, rather than energetic, arguments.

Returning to Uranus and Neptune, we estimate the characteristic value of the poloidal field to be the mean value at the approximate boundary of the dynamos, defined as being the midpoint of the region of decreasing conductivity ($(b-c)/2$ in the notation of equation (15): $0.8R_U$ and $0.75R_N$), giving $B_P \approx 2 \times 10^{-4}$ T, and $B_s = 0.016$ T. This gives $R_m \approx 80^2 = 6400$, and $B_T = 6400 B_P = 1.3$ T. This is a large value for the toroidal field, and it is instructive to consider the associated ohmic heating. If we define the mean toroidal field strength

$$\langle B_T^2 \rangle = \frac{1}{V} \int (\mathbf{B}_T)^2 dV \tag{43}$$

then, by expanding the toroidal field in the spherical decay functions [*Backus*, 1958; *Gubbins*, 1976], we can show

$$W_T = \int (\nabla \wedge \mathbf{B}_T)^2 dV/({\mu_0}^2 \sigma) \geq 84.57 c \langle B_T^2 \rangle/({\mu_0}^2 \sigma) \tag{44}$$

where to allow analytic calculation, we have assumed a uniformly conducting core, radius c. (Note for the toroidal field, the appropriate maximum length scale $\approx c/5$, not the often used $c/3$, which is appropriate for the poloidal field. This estimate of the length scale is a formal upper bound: for a smaller characteristic length, the magnetic heating estimate is increased.) Substituting values in equation (44), we obtain estimates for toroidal heating of 7.9×10^{17} W for Uranus and 8.2×10^{17} W for Neptune. The measured surface heat flows are 3×10^{14} W for Uranus and 3×10^{15} W for Neptune, so in both cases, the calculated ohmic heating bound is several orders of magnitude greater than the observed surface heat flow. It is clear that the assumptions on which this calculation is based are not consistent with the observations.

What if the assumption of strong differential rotation is in error? If we assume only that the dynamo region is in magnetostrophic balance, we must estimate B_T from equation (40), where now the magnetic Reynolds number is unknown. If, as here, the magnetic Reynolds number is defined in terms of large-scale parameters (core radius and mean flow), then it is usually assumed that for dynamo action $R_m \geq 10$ [e.g., *Stacey*, 1992, section 7.2.4]. For $R_m = 10$, $B_T = \sqrt{10} B_s = 0.05$ T, giving an estimate of the toroidal heating for Uranus of 1.2×10^{15} W and for Neptune of 1.25×10^{15} W. The Uranus value exceeds the measured value, while the Neptune value approaches it.

Assuming that the scaling approach is valid (for some reservations, see *Stevenson* [1983]), it thus seems likely that, contrary to the assumption of previous workers [*Hide*, 1988; *Podolak et al.*, 1991], the toroidal field is not in magnetostrophic balance. Physically, the available energy source is insufficient to drive a strong field dynamo, given the high resistivity of the conducting region. *Stevenson* [1984] has considered the possibility of an energetically limited dynamo to explain the field of Mercury, but we are not aware of a dynamical study of this scenario. If instead we assume a weak field dynamo, then we would expect $B_T \sim B_P$ [*Busse*, 1978], in which case there is no explicit problem with the heat flow constraint. However, calculated weak field dynamos have much small-scale magnetic field structure, so that even a weak field state does not ensure that the heat generation constraint is satisfied [*Hide and Roberts*, 1979].

The largest uncertainty in this argument arises from the value of the conductivity: since $B_T \sim \sigma^{-1}$, $W_T \sim \sigma^{-3}$. Thus an order of magnitude increase in the conductivity estimate at higher pressures within the planets would significantly decrease the bound. The experimental shock wave data of *Nellis et al.* [1988] is limited to pressures of up to 1 Mbar, but there are good theoretical reasons to believe that the ionic conductivity will not increase significantly at higher pressures. *Ross* [1981] has suggested the planets may possess a layer of metallic carbon at great depths, although others [e.g., *Podolak et al.*, 1991] consider this unlikely. Further, if, as some [e.g., *Podolak et al.*, 1991] have suggested, the dynamo is located in a thin shell at the outer edge of the icy mantle, then the existence of a highly conductive layer would not be relevant. If the thin shell has thickness Xc, then a scaling estimate for the ohmic dissipation gives

$$W_T \sim \frac{4\pi}{X} c \langle B_T^2 \rangle/({\mu_0}^2 \sigma) \tag{45}$$

which is of the same order as the estimate in equation (44), and therefore similarly unsatisfactory on energetic grounds.

Thus, if we assume that the fields of the Earth, Jupiter, and Saturn are in magnetostrophic balance, but those of Uranus and Neptune are not, then the differences between the fields are less surprising. We might further speculate that the reason for the lack of a dominant dipole field is that the magnetic field is not important in the first-order dynamics, and so the influence of rotation on the field is weaker.

Second we consider the effect of a conducting solid inner core on the dynamo process. It has recently been suggested that the Earth's conducting solid inner core may play a significant role in the dynamics of the fluid outer core and the generation of the geomagnetic field. In studies of an $\alpha\omega$-like dynamo, *Hollerbach and Jones* [1993] found that chaotic oscillations of the field generated in the outer core are stabilized on the diffusive timescale of the solid inner core. A similar effect has also been observed in the fully dynamical calculations of *Glatzmaier and Roberts* [1995a, 1995b]. The range of possible internal structures for Uranus and Neptune allow at one end for iron/silicate cores of up to 1/5 of the planetary radius and at the other for no distinct rocky core [*Hubbard et al.*, 1991]. The Lindemann melting law [*Hubbard*, 1981, 1984] suggests that a rocky core would be solid, but even if iron has differentiated to form a highly conducting solid inner core, this would probably be too small compared with the dynamo region to be important. If a large solid conducting inner core is required to stabilize the magnetic field, then the reversal explanation for the fields of Uranus and Neptune could be partially correct, as they could be varying chaotically with no strongly preferred orientation.

This suggestion also has ramifications for the fields of Jupiter and Saturn. The current data for the field of Jupiter do not suggest main field magnetic secular variation [*Connerney and Acuña*, 1982] (although this issue will be clarified by data from the Galileo space probe), and indirect evidence from ring structure suggests that the Saturnian field might have been stable for over 100 m.y. [*Northrop and Connerney*, 1987]. The temperatures in both planets are too high for hydrogen to exist in a solid metallic phase [*Stevenson and Salpeter*, 1976; *Hubbard*, 1989]. However, if the fields are not generated in the metallic regions, but instead in more weakly conducting regions located above the molecular-metallic phase transition [*Stevenson*, 1983], then the interior metallic region could provide the required stabilizing influence.

We have discussed two possible explanations for field morphologies of Uranus and Neptune. These two hypotheses, an energetically limited dynamo and a chaotically reversing dynamo, are both amenable to investigation by fully dynamical numerical simulation. Numerical simulation is our next line of investigation, given that further data that might resolve secular variation of the Uranus and Neptune will not be forthcoming in the foreseeable future.

Appendix A: Ohmic Heat Flow

We wish to obtain a lower bound for the ohmic heat generation within a planet, radius r, given a particular external potential magnetic field, and a known internal conductivity structure. This is a generalization of the result of *Gubbins* [1975], who considered a core of constant conductivity encased in an insulating mantle. The ohmic heating within a volume can be written

$$W = \int \frac{J^2}{\sigma} dV = \int \frac{(\nabla \wedge \mathbf{B})^2}{\mu_0^2 \sigma} dV \qquad \text{(A1)}$$

We use a poloidal-toroidal decomposition for the field [*Gubbins and Roberts*, 1987]. To match the external field, we need only a poloidal field; thus for the lower bound, we set the toroidal scalar to zero. We write the poloidal field

$$\mathbf{B} = \sum_{l=1}^{\infty} \sum_{m=-l}^{l} \nabla \wedge \nabla \wedge [p_l^m(r) Y_l^m(\theta, \phi)\mathbf{r}] \qquad \text{(A2)}$$

where $Y_l^m(\theta, \phi)$ are fully normalized spherical harmonics, defined such that

$$\oint Y_l^m(\theta, \phi) Y_s^{r*}(\theta, \phi) d\Omega = \delta_{ls}\delta_{mr}. \qquad \text{(A3)}$$

Substituting equation (A2) into equation (A1), after some manipulations, we obtain

$$W = \sum_{l,m} \int_0^a \left\{ \frac{l(l+1)r^2}{\mu_0^2 \sigma(r)} \times \left[\frac{d^2 p_l^m}{dr^2} + \frac{2}{r}\frac{dp_l^m}{dr} - \frac{l(l+1)p_l^m}{r^2} \right]^2 dr \right\} \qquad \text{(A4)}$$

We wish to minimize this functional. Writing

$$Q_l^m = \frac{d^2 p_l^m}{dr^2} + \frac{2}{r}\frac{dp_l^m}{dr} - \frac{l(l+1)p_l^m}{r^2} \qquad \text{(A5)}$$

and solving the Euler-Lagrange equations for Q_l^m, we obtain

$$\begin{aligned} Q_l^m &= \frac{d^2 p_l^m}{dr^2} + \frac{2}{r}\frac{dp_l^m}{dr} - \frac{l(l+1)p_l^m}{r^2} \\ &= \sigma(r)(A_l^m r^l + B_l^m r^{-l-1}) \end{aligned} \qquad \text{(A6)}$$

where A_l^m and B_l^m are arbitrary constants of integration. We set $B_l^m = 0$ by requiring finite currents at $r = 0$. Substituting for Q_l^m in equation (A4),

$$W = \sum_{l,m} (A_l^m)^2 \frac{l(l+1)}{\mu_0^2} \int_0^a \sigma(r) r^{2l+2} dr \qquad \text{(A7)}$$

The constants A_l^m are determined by the external field. Integrating equation (A6),

$$\begin{aligned} p_l^m &= A_l^m r^l \int_0^r (r')^{-2(l+1)} \int_0^{r'} \sigma(r'')(r'')^{2(l+1)} dr'' dr' \\ &\quad + C_l^m r^l + D_l^m r^{-l-1} \end{aligned} \qquad \text{(A8)}$$

C_l^m and D_l^m are further arbitrary constants which define a potential field (i.e., no currents and so no ohmic heating). For finite $\mathbf{B}$ at $r = 0$, $D_l^m = 0$. We must match the internal field $\mathbf{B}$ at $r = a$ to an external potential field, requiring continuity of both p_l^m and dp_l^m/dr.

For a potential field bounded at infinity, with scalar potential

$$\Phi = \sum_{l=1}^{\infty} r^{-l-1} \sum_{m=-l}^{l} E_l^m Y_l^m(\theta, \phi) \tag{A9}$$

the poloidal scalar function is

$$p_l^m = -\frac{E_l^m}{l} r^{-l-1} \tag{A10}$$

For any set of coefficients E_l^m,

$$p_l^m + \frac{r}{l+1}\frac{dp_l^m}{dr} = 0 \tag{A11}$$

Differentiating equation (A8),

$$\frac{dp_l^m}{dr} = \frac{lp_l^m}{r} + A_l^m r^{-l-2} \int_0^r \sigma(r')(r')^{2l+2} dr' \tag{A12}$$

Combining equations (A10) - (A12) gives

$$E_l^m \frac{2l+1}{l} = A_l^m \int_0^a \sigma(r) r^{2l+2} dr \tag{A13}$$

so substituting for A_l^m in equation (A7),

$$W = \sum_{l,m} (E_l^m)^2 \frac{(l+1)(2l+1)^2}{l\mu_0^2} \Big/ \int_0^a \sigma(r) r^{2l+2} dr \tag{A14}$$

It remains only to convert the coefficients E_l^m to the Schmidt normalized coefficients g_l^m and h_l^m in common use in geomagnetism. This gives

$$W = \sum_{l,m} 4\pi a^{2l+4} \frac{(l+1)(2l+1)}{l\mu_0^2} ((g_l^m)^2 + (h_l^m)^2) \Big/ \int_0^a \sigma(r) r^{2l+2} dr \tag{A15}$$

If σ is constant over a core of radius c, we recover the result of *Gubbins* [1975]:

$$W = \frac{4\pi a}{\mu_0^2 \sigma} \sum_{l,m} \left(\frac{a}{c}\right)^{2l+3} \frac{(l+1)(2l+1)(2l+3)}{l} \times [(g_l^m)^2 + (h_l^m)^2] \tag{A16}$$

Appendix B: Upper Bound on the Symmetry Parameter $\hat{f}_2$

We seek the axis (θ_a, ϕ_a) which minimizes

$$\hat{f}_2 = \frac{e_2 - \hat{e}_2^0}{e_2} \tag{B1}$$

and show that the optimized value of $\hat{f}_2$ cannot exceed 1/4. The spherical harmonic potential at a point (θ, ϕ) can be written as a tensor expansion

$$\Phi = D_i n_i + Q_{ij} n_i n_j + O_{ijk} n_i n_j n_k + \ldots \tag{B2}$$

where

$$\mathbf{n} = (\sin\theta\cos\phi, \sin\theta\sin\phi, \cos\theta) \tag{B3}$$

is the unit normal at the point (θ, ϕ), and the terms D_i, Q_{ij}, O_{ijk} are the elements of Cartesian tensors. The dipole coefficients are represented by a vector $\mathbf{D}$ with three independent components, the quadrupole coefficients (in which we are interested here) are represented by a real symmetric, traceless, two-tensor $\mathbf{Q}$ with five independent components, and so on. Equating equation (B2) to equation (1), and taking into account the Schmidt normalization, we may write

$$\mathbf{Q} = \begin{pmatrix} (-g_2^0 + \sqrt{3}g_2^2)/2 & \sqrt{3}h_2^2/2 & \sqrt{3}g_2^1/2 \\ \sqrt{3}h_2^2/2 & (-g_2^0 - \sqrt{3}g_2^2)/2 & \sqrt{3}h_2^1/2 \\ \sqrt{3}g_2^1/2 & \sqrt{3}h_2^1/2 & g_2^0 \end{pmatrix} \tag{B4}$$

As $\mathbf{Q}$ is real symmetric, it may be diagonalized by rotating into the frame of its three orthogonal eigenvectors. Working in this frame,

$$\mathbf{Q} = \begin{pmatrix} (-g_2^0 + \sqrt{3}g_2^2)/2 & 0 & 0 \\ 0 & (-g_2^0 - \sqrt{3}g_2^2)/2 & 0 \\ 0 & 0 & g_2^0 \end{pmatrix} \tag{B5}$$

By either maximizing equation (37), or arguing directly from the elements of the tensor, we may show that the maximum absolute value for $\hat{g}_2^0$ is either $|g_2^0|$ or $\frac{1}{2}(|g_2^0| + \sqrt{3}|g_2^2|)$. Writing $g_2^2 = Ag_2^0$, the corresponding values of $\hat{f}_2$ are

$$\hat{f}_2 = \frac{A^2}{1+A^2}, \quad \frac{(\sqrt{3}-A)^2}{4(1+A^2)} \tag{B6}$$

We wish to obtain the minimum value of $\hat{f}_2$, and so adopt the smaller of these two values. Given this choice, the maximum value occurs at $A = 1/\sqrt{3}$ or $A \to \infty$, when $\hat{f}_2 = 1/4$. In these cases, we may define a reference frame in which the quadrupole field is entirely nonaxial and can be described with a single coefficient g_2^2.

Acknowledgments. J.B. is supported by an NSF Presidential Young Investigator Award (EAR-9158298), and by the Packard Foundation. This work was also supported by NASA awards NAGW-2494 and NAGW-3467. We thank J. E. Connerney and N. F. Ness for assistance with the Voyager II data, and M. Marley for providing us with his recent Uranus and Neptune models. We also thank K. Whaler for useful discussions, and N. F. Ness and D. J. Stevenson for constructive reviews.

References

Backus, G. E., A class of self-sustaining dissipative spherical dynamos, *Ann. Phys*, *4*, 372–447, 1958.

Backus, G. E., Gross thermodynamics of heat engines in deep interior of Earth, *Proc. Natl. Acad. Sci. USA*, *72*, 1555–1558, 1975.

Backus, G. E., Bayesian inference in geomagnetism, *Geophys. J.*, *92*, 125–142, 1988.

Backus, G. E., and F. Gilbert, Numerical applications of a formalism for geophysical inverse problems, *Geophys. J. R. Astron. Soc.*, *13*, 247–276, 1967.

Backus, G. E., and F. Gilbert, The resolving power of gross Earth data, *Geophys. J. R. Astron. Soc.*, *16*, 169–205, 1968.

Backus, G. E., and F. Gilbert, Uniqueness in the inversion of invariant gross Earth data, *Philos. Trans. R. Soc. London A*, *266*, 123–192, 1970.

Behannon, K. W., M. H. Acuña, L. F. Burlaga, R. P. Lepping, N. F. Ness, and F. M. Neubauer, Magnetic field experiment for Voyagers 1 and 2, *Space Sci. Rev.*, *21*, 235–257, 1977.

Benton, E. R., and L. R. Alldredge, On the interpretation of the geomagnetic energy spectrum, *Phys. Earth Planet. Inter.*, *48*, 265–278, 1987.

Bloxham, J., and A. Jackson, Fluid flow near the surface of the Earth's outer core, *Rev. Geophys.*, *29*, 97–120, 1991.

Bloxham, J., D. Gubbins, and A. Jackson, Geomagnetic secular variation, *Philos. Trans. R. Soc. London A*, *329*, 415–502, 1989.

Bullard, E. C., and H. Gellman, Homogeneous dynamos and terrestrial magnetism, *Philos. Trans. R. Soc. London A*, *247*, 213–278, 1954.

Busse, F. H., Introduction to the theory of geomagnetism, in *Rotating Fluids in Geophysics*, edited by P. H. Roberts, and A. M. Soward, pp. 361–388, Academic Press, San Diego, Calif., 1978.

Connerney, J. E. P., The magnetic field of Jupiter: a generalized inverse approach, *J. Geophys. Res.*, *86*, 7679–7693, 1981.

Connerney, J. E. P., Doing more with Jupiter's magnetic field, in *Planetary Radio Emissions III*, edited by H. O. Rucker, S. J. Bauer, and M. L. Kaiser, pp. 13–33, Austrian Acad. of Sci. Press, Vienna, 1992.

Connerney, J. E. P., Magnetic fields of the outer planets, *J. Geophys. Res.*, *98*, 18,659–18,679, 1993.

Connerney, J. E. P., and M. H. Acuña, Jovimagnetic secular variation, *Nature*, *297*, 313–315, 1982.

Connerney, J. E. P., M. H. Acuña, and N. F. Ness, Modeling the Jovian current sheet and inner magnetosphere, *J. Geophys. Res.*, *86*, 8370–8384, 1981.

Connerney, J. E. P., N. F. Ness, and M. H. Acuña, Zonal harmonic model of Saturn's magnetic field from Voyager 1 and 2 observations, *Nature*, *298*, 44–46, 1982.

Connerney, J. E. P., M. H. Acuña, and N. F. Ness, The magnetic field of Uranus, *J. Geophys. Res.*, *92*, 15,329–15,336, 1987.

Connerney, J. E. P., M. H. Acuña, and N. F. Ness, The magnetic field of Neptune, *J. Geophys. Res.*, *96*, 19,023–19,042, 1991.

Connerney, J. E. P., R. Baron, T. Satoh, and T. Owen, Images of excited H_3^+ at the foot of the Io flux tube in Jupiter's atmosphere, *Science*, *262*, 1035–1038, 1993.

Constable, C. G., and R. L. Parker, Smoothing, splines and smoothing splines: Their application in geomagnetism., *J. Comput. Phys.*, *78*, 493–508, 1988.

Constable, C. G., and R. L. Parker, Deconvolution of long-core paleomagnetic measurements – Spline therapy for the linear problem, *Geophys. J. Int.*, *104*, 453–468, 1991.

Davis, L., Jr., and E. J. Smith, A model of Saturn's magnetic field based on all available data, *J. Geophys. Res.*, *95*, 15237–15261, 1990.

de Boor, C., *A Practical Guide to Splines*, Springer-Verlag, New York, 1978.

Glatzmaier, G. A., and P. H. Roberts, A three-dimensional convective dynamo solution with rotating and finitely conducting inner core and outer mantle, *Phys. Earth Planet Inter.*, *91*, 63–75, 1995a.

Glatzmaier, G. A., and P. H. Roberts, A three-dimensional self-consistent computer simulation of a geomagnetic field reversal, *Nature*, *377*, 203–209, 1995b.

Gubbins, D., Can the Earth's magnetic field be sustained by core oscillations?, *Geophys. Res. Lett.*, *2*, 409–412, 1975.

Gubbins, D., Observational constraints on the generation process of the Earth's magnetic field, *Geophys. J. R. Astron. Soc.*, *47*, 19–39, 1976.

Gubbins, D., Energetics of the Earth's core, *J. Geophys.*, *43*, 453–496, 1977.

Gubbins, D., Geomagnetic field analysis – I. Stochastic inversion, *Geophys. J. R. Astron. Soc.*, *73*, 641–652, 1983.

Gubbins, D., and J. Bloxham, Geomagnetic field analysis – III. Magnetic fields on the core-mantle boundary, *Geophys. J. R. Astron. Soc.*, *80*, 695–713, 1985.

Gubbins, D., and N. Roberts, Use of the frozen flux approximation in the interpretation of archaemagnetic and palaeomagnetic data, *Geophys. J. R. Astron. Soc.*, *73*, 675–687, 1983.

Gubbins, D., and P. H. Roberts, Magnetohydrodynamics of the Earth's core, in *Geomagnetism*, edited by J. A. Jacobs, vol. 2, chap. 1, Academic, San Diego, Calif., 1987.

Gubbins, D., T. G. Masters, and J. A. Jacobs, Thermal evolution of the Earth's core, *Geophys. J. R. Astron. Soc.*, *59*, 57–100, 1979.

Hewitt, J. M., D. P. McKenzie, and N. O. Weiss, Dissipative heating in convective flows, *J. Fluid Mech.*, *68*, 721–738, 1975.

Hide, R., Towards an interpretation of Uranus's eccentric magnetic field, *Geophys. Astrophys. Fluid Dyn.*, *44*, 207–209, 1988.

Hide, R., and P. H. Roberts, How strong is the magnetic field in the Earth's liquid core?, *Phys. Earth Planet. Inter.*, *20*, 124–126, 1979.

Hollerbach, R., and C. A. Jones, Influence of the Earth's inner core on geomagnetic fluctuations and reversals, *Nature*, *365*, 541–543, 1993.

Holme, R., and J. Bloxham, Alleviation of the Backus effect in geomagnetic field modelling, *Geophys. Res. Lett.*, *22*, 1641–1644, 1995.

Hubbard, W. B., Constraints on the origin and interior structure of the major planets, *Philos. Trans. R. Soc. London A*, *303*, 315–326, 1981.

Hubbard, W. B., *Planetary Interiors*, Van Nostrand Reinhold, New York, 1984.

Hubbard, W. B., Structure and composition of giant planet interiors, in *Origin and Evolution of Planetary and Satellite Atmospheres*, edited by S. K. Atreya, J. B. Pollack, and M. S. Matthews, pp. 539–563, Univ. of Ariz. Press, Tuscon, 1989.

Hubbard, W. B., and J. J. MacFarlane, Structure and evolution of Uranus and Neptune, *J. Geophys. Res.*, *85*, 225–234, 1980.

Hubbard, W. B., W. J. Nellis, A. C. Mitchell, N. C. Holmes, S. S. Limaye, and P. C. McCandless, Interior structure of Neptune: Comparison with Uranus, *Science*, *253*, 648–651, 1991.

Ladreiter, H. P., Y. Leblanc, G. K. F. Rabl, and H. O. Rucker, Emission characteristics and source location of the smooth Neptunian kilometric radiation, *J. Geophys. Res.*, *96*, 19,101–19,110, 1991.

Lanczos, C., *Linear differential operators*, chap. 3, Van Nostrand Rheinhold, New York, 1961.

Langel, R. A., The main field, in *Geomagnetism*, edited by J. A. Jacobs, vol. 1, chap. 4, Academic, San Diego, Calif., 1987.

Langel, R. A., and R. H. Estes, A geomagnetic field spectrum, *Geophys. Res. Lett.*, *9*, 250–253, 1982.

Lindal, G. F., J. R. Lyons, D. N. Sweetnam, V. R. Eshleman, D. P. Hinson, and G. L. Tyler, The atmosphere of Uranus: Results of radio occultation measurements with Voyager 2, *J. Geophys. Res.*, *92*, 14987–15001, 1987.

Lowes, F. J., Mean-square values on the sphere of spherical harmonic vector fields, *J. Geophys. Res.*, *71*, 2179, 1966.

Lowes, F. J., Spatial power spectrum of the main geomagnetic field, and extrapolation to the core, *Geophys. J. R. Astron. Soc.*, *36*, 717–730, 1974.

Mao, H. K., and R. J. Hemley, Optical studies of hydrogen above 200GPa: Evidence for metallization by band overlap, *Science*, *244*, 1462–1465, 1989.

Mauersberger, P., Das mittel der energiedickhte des geomagnetischen hauptfeldes an der erdoberflasche and seine säkulare änderung, *Gerlands Beitr. Geophys.*, *65*, 207–215, 1956.

Nellis, W. J., D. C. Hamilton, N. C. Holmes, H. B. Radousky, F. H. Ree, A. C. Mitchell, and M. Nicol, The nature of the

interior of Uranus based on studies of planetary ices at high dynamic pressure, *Science*, *240*, 779–781, 1988.

Ness, N. F., K. W. Behannon, R. P. Lepping, and K. H. Schatten, Use of two magnetometers for magnetic field measurements on a spacecraft, *J. Geophys. Res.*, *76*, 3564–3573, 1971.

Ness, N. F., M. H. Acuña, K. W. Behannon, L. F. Burlaga, J. E. P. Connerney, R. P. Lepping, and F. M. Neubauer, Magnetic fields at Uranus, *Science*, *233*, 85–89, 1986.

Ness, N. F., M. H. Acuña, L. F. Burlaga, J. E. P. Connerney, R. P. Lepping, and F. M. Neubauer, Magnetic fields at Neptune, *Science*, *246*, 1473–1477, 1989.

Northrop, T. G., and J. E. P. Connerney, A micrometeorite erosion model and the age of Saturn's rings, *Icarus*, *70*, 124–137, 1987.

Pearl, J. C., and B. J. Conrath, The albedo, effective temperature, and energy balance of Neptune, as determined from Voyager data, *J. Geophys. Res.*, *96*, 18,921–18,930, 1991.

Podolak, M., R. T. Reynolds, and R. Young, Post Voyager comparisons of the interiors of Uranus and Neptune, *Geophys. Res. Lett.*, *17*, 1737–1740, 1990.

Podolak, M., W. B. Hubbard, and D. J. Stevenson, Models of Uranus' interior and magnetic field, in *Uranus*, edited by J. T. Bergstrahl, E. D. Miner, and M. S. Matthews, pp. 29–61, University of Arizona Press, Tuscon, 1991.

Podolak, M., A. Weizmann, and M. Marley, Comparative models of Uranus and Neptune, *Planet. Space Sci.*, in press, 1995.

Rädler, K.-H., and N. F. Ness, The symmetry properties of planetary magnetic fields, *J. Geophys. Res.*, *95*, 2311–2318, 1990.

Ross, M., The ice layer in Uranus and Neptune – Diamonds in the sky?, *Nature*, *292*, 435–436, 1981.

Russell, C. T., Magnetic fields of the terrestrial planets, *J. Geophys. Res.*, *98*, 18,681–18,695, 1993.

Ruzmaikin, A. A., and S. V. Starchenko, On the origin of Uranus and Neptune magnetic fields, *Icarus*, *93*, 82–87, 1991.

Schulz, M., and G. A. Paulikas, Planetary magnetic fields: A comparative view, *Adv. Space Res.*, *10*, 155–164, 1990.

Shure, L., R. L. Parker, and G. E. Backus, Harmonic splines for geomagnetic modelling, *Phys. Earth Planet. Inter.*, *28*, 215–229, 1982.

Stacey, F. D., *Physics of the Earth*, Brookfield, Brisbane, 1992.

Stevenson, D. J., Interiors of the giant planets, *Annu. Rev. Earth Planet. Sci.*, *10*, 257–295, 1982.

Stevenson, D. J., Planetary magnetic fields, *Rep. Prog. Phys.*, *46*, 555–620, 1983.

Stevenson, D. J., The energy flux number and three types of planetary dynamo, *Astron. Nachr.*, *305*, 257–264, 1984.

Stevenson, D. J., and E. E. Salpeter, Interior models of Jupiter, in *Jupiter*, edited by T. Gehrels, pp. 85–112, Univ. of Ariz. Press, Tuscon, 1976.

Tyler, G. L., et al., Voyager radio science observations of Neptune and Triton, *Science*, *246*, 1466–1473, 1989.

Wessel, P., and W. H. F. Smith, Free software helps map and display data, *Eos Trans. AGU*, *72*, 445–446, 1991.

Whaler, K. A., and D. Gubbins, Spherical harmonic analysis of the geomagnetic field: an example of a linear inverse problem, *Geophys. J. R. Astron. Soc.*, *65*, 645–693, 1981.

J. Bloxham, Department of Earth and Planetary Sciences, Harvard University, Cambridge, MA 02138.

R. Holme, Department of Geology and Geophysics, University of Edinburgh, Grant Institute, West Mains Road, Edinburgh EH9 3JW, Scotland. (email: holme@mail.glg.ed.ac.uk)

(Received July 14, 1995; revised October 30, 1995; accepted November 7, 1995.)